Engineering Fracture Mechanics 328 (2025) 111584

Contents lists available at ScienceDirect

Engineering Fracture Mechanics

journal homepage: www.elsevier.com/locate/engfracmech

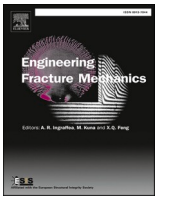

Temperature-dependent fracture characterization of methacrylate adhesive-bonded glass fibre-reinforced reactive thermoplastic composites

Milos Zivkovic [a], Erli Shi [a], Wilfried V. Liebig [b], John Montesano [a,*]

[a] Composites Research Group, Department of Mechanical & Mechatronics Engineering, University of Waterloo, Waterloo, Canada
[b] Institute for Applied Materials - Materials Science and Engineering (IAM-WK), Karlsruhe Institute of Technology, Karlsruhe, Germany

ARTICLE INFO

Keywords:
Fibre-reinforced reactive thermoplastics
Methyl methacrylate adhesive
Fracture assessment
Low temperature

ABSTRACT

The Mode I and Mode II fracture behaviour of glass fibre-reinforced reactive thermoplastics bonded with a methyl methacrylate adhesive was characterized under room temperature (RT) and low temperature (LT; –40 °C) conditions via double cantilever beam (DCB) and end-notch flexural (ENF) tests at varying bond-line thicknesses. RT-DCB specimens exhibited a higher peak force, lower elastic stiffness, and higher initiation fracture toughness (77 % increase for thickest bond line) compared to LT-DCB specimens. Mode I initiation fracture toughness was insensitive to bond-line thickness at RT but decreased with increasing bond-line thickness at LT. RT-DCB specimens exhibited stable ductile cohesive failure. Conversely, LT-DCB specimens exhibited unstable oscillatory crack propagation between the substrates which was influenced by the substrate microstructure and caused by thermally-induced residual stresses in the adhesive layer. RT-ENF specimens exhibited higher peak force and a positive correlation with bond-line thickness, while LT-ENF specimens showed a negative correlation with bond-line thickness. All RT-ENF specimens were characterized by ductile cohesive fracture with consistent hackle formations, while LT-ENF specimens experienced brittle failure within the substrate characterized by fibre pullout and shear cusps between fibres. The fracture characterization results presented can contribute to optimizing the damage tolerance of corresponding adhesive-bonded components.

1. Introduction

The increased usage of fibre-reinforced thermoplastics for load-bearing structures has been driven in part by sustainability initiatives across different sectors. Specifically in the wind energy sector, thermoplastic-based composites offer increased end-of-life recyclability pathways for large wind turbine blades when compared to those manufactured using conventional thermosetting-based composites. Thermoplastics also exhibit superior damage tolerance characteristics and impact properties when compared to common thermosetting polymers such as epoxy [1,2]. Wind turbine blade structures, including small-scale blades which are the intended application of the study herein, are typically manufactured using vacuum infusion processes, which are not conducive for current fibre-reinforced thermoplastic material systems. However, recent advancements in the development of new reactive thermoplastics with low viscosities has enabled the fabrication of blade structures using vacuum infusion processes [3]. Recent studies

* Corresponding author.
E-mail address: john.montesano@uwaterloo.ca (J. Montesano).

https://doi.org/10.1016/j.engfracmech.2025.111584
Received 1 July 2025; Received in revised form 19 September 2025; Accepted 25 September 2025
Available online 26 September 2025

Nomenclature

English Alphabet

a	Crack length
a_0	Pre-crack length
b	Width of joint
C	Beam compliance
E_1	Longitudinal Young's modulus
E_2, E_3	Transverse Young's modulus
E_s	Tensile modulus
G_{12}, G_{13}	In-plane shear modulus
G_{23}	Out-of-plane shear modulus
G_{I}	Mode I strain energy release rate
G_{IC}	Mode I critical energy release rate
G_{IIC}	Mode II critical energy release rate
h	Thickness of beam substrate
L	Beam length
m	SBT calculation variable
P	Load
t	Bond-line thickness
X_t	Longitudinal tensile strength
Y_t	Transverse tensile strength

Greek Alphabet

α	Thermal expansion coefficient
α_1	Longitudinal thermal expansion coefficient
α_2	Transverse thermal expansion coefficient
Δ	Compliance correction factor
δ	Load-line displacement
ν_{12}, ν_{13}	Major in-plane Poisson's ratio
ν_{23}, ν_{32}	Minor in-plane Poisson's ratio

Acronyms

ANOVA	Analysis of variance
CTE	Coefficient of thermal expansion
DCB	Double cantilever beam
ENF	Edge notch flexure
FPZ	Fracture process zone
FRP	Fibre-reinforced plastic
LT	Low temperature
MBT	Modified beam theory
MMA	Methyl methacrylate adhesive
PMMA	Polymethyl methacrylate
RT	Room temperature
SBT	Simple beam theory
SERR	Strain energy release rate
UD-NCF	Unidirectional non-crimp fabric
VARTM	Vacuum-assisted resin transfer molding

[4,5] have found that reactive thermoplastics may exhibit superior fracture toughness and damage tolerance characteristics at low ambient temperatures when compared to epoxy systems. This characteristic is particularly advantageous for wind turbines operating in arctic conditions, which is the intended application for the materials studied herein, where ambient temperatures can reach levels below –40 °C. In particular, unidirectional non-crimp fabric (UD-NCF) glass fibre-reinforced reactive thermoplastic composites offer high specific strength and greater anisotropic property tailorability when compared to more conventional woven fabric-based composites, making them ideal candidates for structural components in wind turbine blades.

Fabrication of wind turbine blade structures requires joining of different components using adhesives, which is preferred over alternative joining methods such as mechanical fasteners or thermal welding. Adhesive joints can be tailored to a variety of substrate surfaces and exhibit contrasting mechanical properties depending on their formulations. Depending on the application, adhesives with varying stiffnesses may be used to prioritize strength or minimize stress concentrations at the substrate interfaces, while modern solutions may even combine multiple adhesives within a single joint to leverage these contrasting behaviors [6]. Compared to

thermosets, thermoplastic substrates pose greater challenges with adhesive joining due to their inherent hydrophobicity [7], which can lead to interfacial failure rather than cohesive failure and, thus, a lower bonding strength. This problem is exacerbated when bonding thermoplastic composite substrates with standard epoxy (thermoset) adhesives due to material incompatibility. Various substrate treatments can be performed to increase surface energy, promote mechanical interlocking, and remove contaminants, including solvent degreasing, abrasion, acid etching, and plasma treatments, while peel plies can be used during substrate processing to promote surface roughening [8,9,10,11]. For instance, in the case of plasma treatment, the formation of polar groups (carbonyl, carboxyl, and hydroxyl) on the surface reduce surface tension, improving the bond between the polymer substrate and the adhesive [10]. While abrasion treatments are typically suitable for thermoset composite substrates, they are often insufficient for thermoplastic composites bonded with epoxy adhesives since the abrasion procedure is not as effective at breaking the polymer chains on the substrate surface to encourage chemical adhesion [8].

The diffusivity of an adhesive will often dictate the strength of the bonding interface. Diffusion occurs when adhesive molecules penetrate the substrate and form a new layer that is not identical to either bulk composition [9]. The low rate of diffusivity of an epoxy adhesive into a thermoplastic polymer limits the total amount of intermolecular diffusion, resulting in an insufficient concentration of epoxide groups to be formed that could react with the thermoplastic substrate. An alternative to conventional epoxy adhesives for structural bonding of thermoplastic materials are methyl methacrylate (MMA) adhesives [12]. Due to their higher rate of diffusivity, MMA adhesives can easily etch the surface of thermoplastic materials [13]. MMA adhesives undergo a variant of solvent cementing where the methacrylate monomer (instead of a solvent) can be used to dissolve the MMA substrate before polymerizing in the joint, allowing for high interfacial strength over large surface areas. Therefore, MMA adhesives are compatible with oily and greasy surfaces and provide high interfacial strength and fast processing due to their rapid polymerization rates [14,15,16,17]. MMA adhesives have additional benefits including the ability to cure at room temperature while retaining non-slump properties during processing. Combined with an ability to achieve a “green strength” quickly, this allows parts to be moved and stored as the adhesive cures without sliding and affecting the final alignment [14]. MMA adhesives have recently been considered for use in manufacturing fibre-reinforced thermoplastic wind turbine blades due to their limited surface pre-treatment requirements [14,18,19,20].

The fracture toughness of adhesive joints is required for structural analysis [21] and is typically characterized using double-cantilever beam (DCB) (Mode I) and end-notched flexural (ENF) (Mode II) tests [22,23]. Several studies have been performed that have focused on characterizing the fracture toughness of composites bonded with thermoplastic adhesives. The performance of thermoplastic composite joints bonded with acrylic adhesives has been shown to provide comparable performance to various thermoplastic welding processes [3,24,25], and increased performance compared to epoxy adhesive-bonded counterparts [12]. Devine et al. [24] found that Plexus MA310 methacrylate adhesive provided good compatibility with acrylic-matrix composites, confirming observations from Murray et al. [3]. Investigating the effects of pressure and weld time on ultrasonic welds, Bhudolia et al. [25] recorded a higher lap shear strength for joints bonded with Bostik SAF 30 5 acrylic adhesive than the average welded joint, although optimized weld parameters yielded better peak performance. Similarly, Reis et al. [26] found that a carbon-reinforced polyamide-6 substrate bonded with two-part 3MTM DP8805 NS acrylic adhesive demonstrated a strong bonding resistance in pure Mode II loading even for low energy thermoplastic composite surfaces. Probing the effects of elevated temperature on the same Plexus MA310 methacrylate adhesive used in Refs. [18,24], Moller et al. [27] observed that the Mode I strength decreased by 14 % at 50 °C and 26 % at 80 °C compared to a reference value at 20 °C. Thus, the working temperature must be considered when selecting an appropriate adhesive system due to the dissimilar coefficients of thermal expansion (CTE) between the adhesive and the substrate and the changing mechanical properties of the adhesive with temperature [28].

The fracture behaviour of adhesive-bonded composite joints is undoubtedly influenced by low ambient temperature conditions, and multiple studies have investigated the effects of reduced (including cryogenic) temperatures on epoxy adhesive performance [28,29,30,31,32,33]. Takayuki et al. [29] tested a variety of epoxy adhesives at cryogenic temperatures and attributed the poor performance of AF163-2 K epoxy adhesive film in Mode I and Mode II loading to CTE incompatibility with the CFRP substrate. Zhang et al. [30] found that the load-elongation response of double lap CFRP joints bonded with epoxy adhesive were more influenced by the thermomechanical behaviour of the adhesive than the substrate with a particular sensitivity around the glass transition temperature T_g. Additional studies [31,34] have noted the increasing trends in ultimate strength, yield strength, and elastic modulus with decreasing temperature below T_g. However, Brito et al. [32] performed tests on as-received and hygrothermally aged epoxy-bonded samples and found that the failure mechanism transitioned from cohesive to substrate fibre-tear failure, with the conclusion that the aging process had a comparatively larger affect than the test temperature. Abdel-Monsef et al. [33,35] found similarly pronounced effects of ageing in both Mode I and Mode II crack resistance, while Yildirim et al. [36] found that bonded thermoplastic PEEK composites at low temperature conditions exhibited reduced Mode I toughness but enhanced Mode II toughness. A separate study from Senol et al. [37] on the effects of surface treatment on Mode I and Mode II fracture resistance found a comparatively stronger influence of plasma treatment on Mode II resistance since shear loading was more influenced by the higher chemical functionality.

Similarly, the influence of bond-line thickness on the fracture toughness and overall performance of adhesive bonded joints has been widely studied, with contradictory results [38,39,40,41]. Classical elastic theory predicts that an increase in the bond-line thickness should translate to an increase in the joint strength, but many experimental studies do not support this analysis [39,41]. This discrepancy in performance has been variously attributed to the size effect (since thicker bond-lines have increased likelihood for voids and microcracks) and increased interface stresses caused by rapid spreading of the adhesive at larger bond-line thicknesses [38,40]. Such contradictions have been linked to intrinsic behaviors that broadly follow two generic trends: (1) Type-A adhesives that demonstrate a monotonic increase in fracture energy with bond-line thickness up to a threshold, and (2) Type-B adhesives where the fracture energy increases with bond-line thickness up to a maximum before reducing towards a threshold value [42]. Such an optimum

value within Type-B adhesives can be rationalized as the adhesive experiencing a three-dimensional stress state caused by geometric and material discontinuities [43]. Arenas et al. used a Weibull distribution to assess the reliability of adhesive joints and determine an optimized adhesive thickness [39]. It was observed that for thicknesses between 0.4 and 0.8 mm, the failure mode during shear loading is cohesive and the strength increases as the thickness decreases due to the size effect and interface stresses. However, below a layer thickness of 0.4 mm, the distribution of the sample failure modes gradually transitions from cohesive to adhesive. Thus, the objective for adhesive joint design is minimizing the bond-line thickness while ensuring the joint fails in a cohesive manner. Conversely, Type-A adhesives generally exhibit pronounced ductility, and an increasing bond-line thickness is beneficial for creating a larger volume for energy dissipation [44]. For instance, da Silva et al. [45] compared the Mode II fracture behavior of brittle (Araldite AV138/HV998) and ductile (Araldite 2015) adhesives and found that the energy release rate increases readily with bond-line thickness only in the ductile case due to the pronounced development of the fracture process zone (FPZ). Castagnetti et al. observed that an MMA adhesive undergoing cohesive failure experiences an increasing static strength as the adhesive thickness decreases from 0.4 mm (6 MPa) to 0.05 mm (20 MPa) [46]. This discrepancy was attributed to the MMA adhesive undergoing an incomplete polymerization at higher thicknesses due to an inadequate ratio between the activator and adhesive.

Compared to studies with epoxy adhesive, fewer studies have focused on characterizing the fracture behaviour of composite joints bonded with thermoplastic adhesives at low temperatures. Using a scanning electron microscope (SEM) to investigate the post-mortem fracture surface, Nam et al. [47] reported that ductile polyurethane adhesives can become brittle at cryogenic temperatures. Jia et al. [48,49,50] investigated the Mode I and Mode II fracture toughness of steel substrates bonded with a ductile polyurethane adhesive, where it was observed that the low temperature fracture toughness during Mode I quasi-static loading was approximately 33 % of the value at room temperature. The crack resistance was further reduced to 15 % of the room temperature value at elevated loading rates [48]. However, Jia et al. [50] also found that the Mode II fracture toughness of the polyurethane adhesive at low temperatures was 130 % of the room temperature value, while a follow-up study reported a reduction in shear strength with decreasing temperature [49]. Fractographic observations were not reported in Refs. [48,49,50]. The interplay between bond-line thickness, strain rate, and temperature in a polyurethane adhesive bonded joint was further investigated by Ribas et al. [51], who noted less variation in strain rate sensitivity at reduced temperatures. Without probing the cryogenic behaviour, Hayashi et al. [52] conducted tests on a variety of two-part structural acrylic adhesives (Hardloc C355-20A/B, Hardloc NS700M-20A/B, and Scotch-Weld DP-8810NS Green) and found that the stress–strain relations were highly dependent upon external parameters. While the bulk behaviour of the adhesives obeyed time–temperature superposition principles (increase in maximum stress and decrease in elongation at lower temperatures and higher loading rates), the fracture toughness increased with a combination of higher temperatures and loading rates. Upon reviewing the literature, no study has assessed the Mode I and Mode II fracture behaviour and fracture surface morphology of MMA adhesive-bonded thermoplastic composites at low temperatures.

The goal of this study was to characterize the Mode I and Mode II fracture response of a UD-NCF glass fibre-reinforced reactive polymethyl methacrylate (PMMA) composite bonded with an MMA adhesive under room temperature (RT) and low temperature (LT; –40 °C) conditions. Double cantilever beam (DCB) and end-notch flexural (ENF) tests were conducted on specimens with three different bond line thicknesses to capture the influence on the fracture response. An in-depth assessment of the specimen fracture surface morphology was performed using optical microscopy.

2. Materials and specimen Preparation

2.1. Adherend and adhesive

The composite adherends in this study consisted of a glass fibre UD-NCF reinforcement impregnated with an in-situ polymerizable thermoplastic acrylic matrix. The matrix consisted of Elium 188 XO polymethyl methacrylate (PMMA) resin (Arkema, France) with 2.5 % by-weight of Luperox AFR40 peroxide initiator (Sigma Aldrich, USA) with a post-polymerization dry-Tg of 120 °C [53]. The reinforcement consisted of a commercially available E-glass fibre UD-NCF (Saertex, USA) composed of NEG 2026 E-glass fibre tows with a linear density of 2400 tex and a width of 3.42 mm, stitched together with warp-knitted polyester yarns (110 dtex) in a tricot

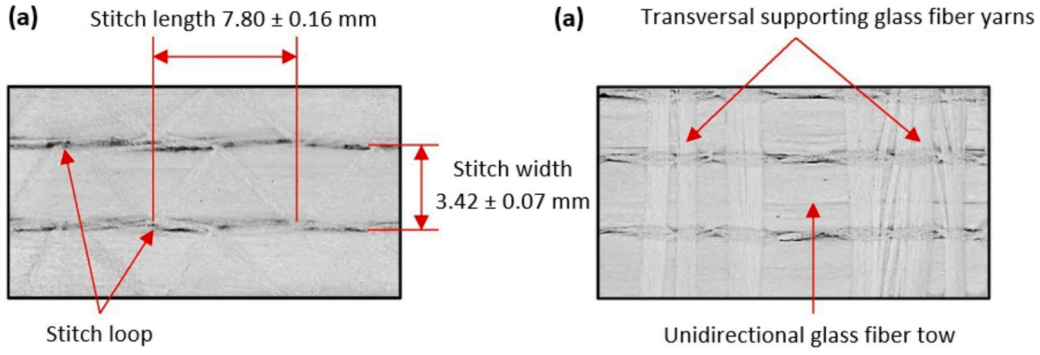

Fig. 1. Schematic of UD-NCF showing (a) tow dimensions, and (b) transversal supporting glass fibre yarns.

pattern (Fig. 1a). The UD-NCF also incorporated supporting NEG 2026 glass fibre yarns (275 tex) transversely to maintain integrity during manufacturing (Fig. 1b). The total areal density of the fabric was 943 g/m^2.

The adherend panels were manufactured via vacuum-assisted resin transfer molding (VARTM) as shown schematically in Fig. 2. An aluminum plate was used as the lower rigid mold and prepared with Frekote PMC cleaner and sealed with Frekote B-15 sealer before applying several coats of Loctite® Frekote 770-NC release agent (Henkel, Germany). Four layers of the UD-NCF fabric, each cut to dimensions of 305 mm × 305 mm, were used for the adherend panels in an $[0]_4$ layup stacking sequence. A peel ply and distribution medium were placed on the dry fabric preform and sealed with a vacuum bag and sealant tape. A Leybold Trivac D30A vacuum pump (Leybold, Germany) was used to evacuate air from the mold under a maximum vacuum pressure of 0.1 mbar prior to a 25 min leak test to ensure the integrity of the vacuum seal. Further details of the panel infusion process are outlined in [54]. Once the fabric stack was fully-impregnated, the laminate was allowed to polymerize for three-hours at room temperature (RT) conditions prior to demolding. The thickness of each substrate was measured with a Mitutoyo micrometer with an average value of 2.91 ± 0.025 mm. The fibre volume fraction of the panels was determined by assessing cross-sectional images of samples using an optical method and found to be approximately 46.2 ± 1.2 % [54]. The mechanical properties of the glass fibre/PMMA composite material required in this study for fracture test data reduction are reported in Table 1.

The MMA adhesive used in this study was FIT30 45 (Bostik, France), which comprised 40 % – 80 % methyl methacrylate monomer, enabling a chemical bond with the composite substrate [55]. The FIT30 45 adhesive also contained smaller quantities of quartz, butyl methacrylate, and isocyanate compounds. The adhesive was dispensed via mixing nozzle with a 10:1 mixing ratio between monomer and initiator.

2.2. Specimen Preparation

The specimen substrates were cut from the fabricated glass fibre/thermoplastic panels using an abrasive water jet cutting machine (ProtoMAX, OMAX), with the fibres oriented along the substrate length. The dimensions of the DCB substrates were 25.4 mm × 140 mm, while the ENF substrate dimensions were 25.4 mm × 150 mm. Prior to bonding the substrates, both surfaces were treated to minimize the presence of contaminants and to achieve an adequate surface roughness. The mold side of the substrates were abraded with 180-grit sandpaper for 2 min, then degreased with isopropanol. The vacuum bag side of the substrates were only degreased with isopropanol, which was sufficient due to the imprint from the peel ply caused during panel processing. A Surtronic 25 profilometer (Taylor Hobson, England) was used to measure the surface roughness of the abraded side of the substrates at three different locations. The average surface roughness (R_A) increased from 0.28 μm to 0.76 μm after abrasion as shown in Table 2. The measured R_A values agreed with the values of 0.88 μm reported by Yildirim et al. [10].

A custom alignment fixture [21] (shown in Fig. 3) was used to bond the peel ply side of one substrate to the mold side of another with the MMA adhesive at ambient conditions of 25 °C and 30 % humidity. Shims were used to define the pre-crack and control the adhesive bond-line thickness. The fixture contained three rows of bolts that were tightened to varying degrees to ensure that the substrates were securely resting on the shims without excessive adhesive squeeze-out. Shoulder bolts within the fixture design ensured parallelism of the substrates. The setup allowed for dispensing of the adhesive system within the 20–40 min Open Time allotted by the TDS [55]. The adhesive joint was allowed to polymerize overnight (at least 15 h prior to removal from the fixture) at the same 25 °C and 30 % humidity conditions as the bonding process without degassing, pressure control, or post curing. Since a stated aim of the blade manufacturing process was cost effectiveness, such energy-intensive curing processes were not deemed applicable. No tests were performed within the 24 h polymerization period specified by the TDS [55].

Three different shim thicknesses were used for DCB (0.25 mm, 0.635 mm, 0.8 mm) and ENF (0.25 mm, 0.475 mm, 0.625 mm) specimens that satisfy both structural requirements for small-scale wind turbine applications [56] and large-scale turbine blade validation [57,58]. After adhesive polymerization was completed, the excess adhesive was removed from the edges of the specimens using a chisel. The bond-line thicknesses and pre-crack lengths were measured using a VHX 5000 opto-digital microscope (Keyence, Canada). An image of the edge of a DCB specimen captured with the microscope with a measurement of the bond line thickness is shown in Fig. 4. The dimensions of the DCB and ENF specimens are presented in Table 3 and Table 4, with reference to the dimensions outlined in Fig. 5.

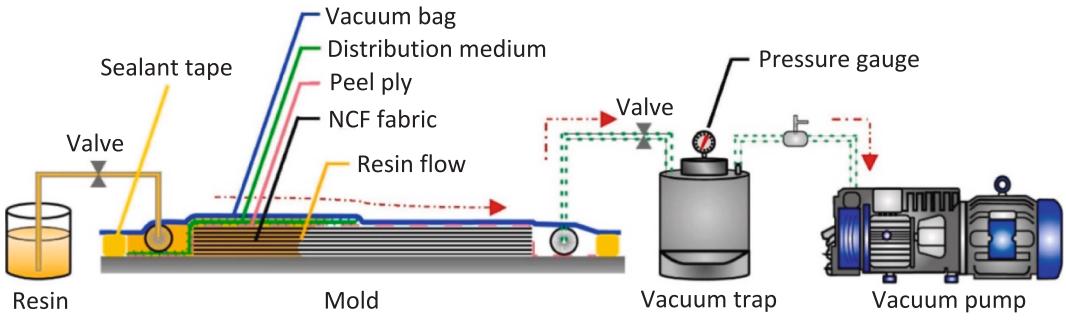

Fig. 2. Schematic of VARTM process used for substrate manufacturing.

Table 1
UD-NCF glass fibre/PMMA mechanical properties [53].

Parameter	Description	Value (RT)	Value (−50 °C)
E_1 (GPa)	Longitudinal Young's modulus	37.76 ± 0.33	38.89 ± 1.21
E_2 (GPa)	Transverse Young's modulus	12.88 ± 0.21	17.43 ± 0.69
ν_{12}	Major in-plane Poisson's ratio	0.229 ± 0.003	0.217 ± 0.008
G_{12} (GPa)	In-plane shear modulus	6.00 ± 0.10	9.05 ± 0.82
X_t (MPa)	Longitudinal tensile strength	1032.88 ± 34.33	1116.71 ± 45.25
Y_t (MPa)	Transverse tensile strength	81.34 ± 6.95	100.21 ± 3.22

Table 2
Surface roughness R_A measurements after mechanical abrasion treatment on mold side of representative substrates.

Sample #	R_A (µm)
1	0.68
	0.69
2	0.93
	0.79
3	0.89
	0.63
4	0.70
	0.79
5	0.81
	0.74
Surface Roughness (prior to abrasion) (µm)	0.28
Average Surface Roughness ± STV (µm)	0.764 ± 0.0469

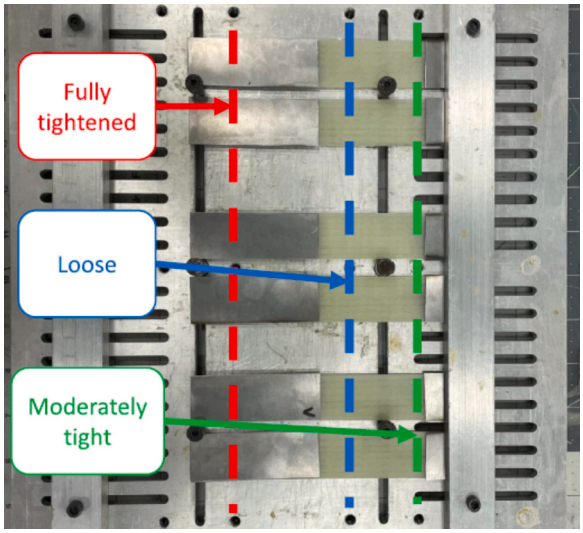

Fig. 3. Custom fixture used for bonding DCB and ENF samples to a prescribed bondline thickness.

The grips of the test frame used in this study (Section 3.1) necessitated the use of piano hinges bonded onto the DCB specimens to enable the application of a tensile load to drive crack propagation as per ASTM standard D5528 [22]. Stainless steel piano hinges (Spaenaur, Canada) with 2.29 mm (0.090 in) thick arms and a 4.75 mm (0.187 in) diameter hinge pin were used to ensure that peeling of the hinges from the substrates was mitigated. The surfaces of the substrates were locally sand blasted (60-grit silicon carbide at 172 kPa) and cleaned with isopropanol prior to bonding with the piano hinges. The hinges were bonded to the substrates using Loctite 480 (Henkel, USA) and allowed to cure for 24 h at room temperature while clamped to achieve full strength.

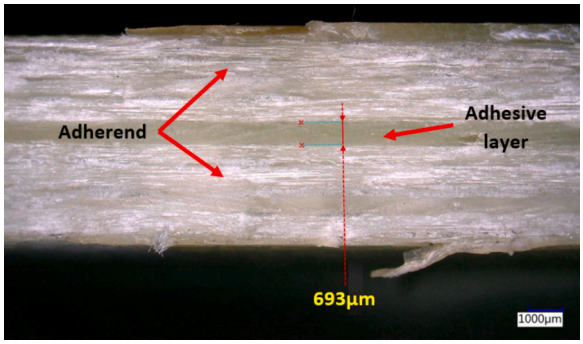

Fig. 4. Image of bonded specimen with bond-line thickness measurement.

Table 3
DCB test specimen dimensions (corresponding to Fig. 5a).

Shim thickness (mm)	Length, L (mm)	Width, b (mm)	Bond-line Thickness, t (mm) (Avg ± STV)	Pre-Crack Shim length, a_0 (mm) (Avg ± STV)	Total Sample Thickness, 2 h (mm) (Avg ± STV)	Average Surface Roughness (µm) (Avg ± STV)
0.25	140	25	0.33 ± 0.049	45.52 ± 0.44	6.01 ± 0.088	0.76 ± 0.047
0.64			0.72 ± 0.12	45.41 ± 0.47	6.35 ± 0.065	
0.8			0.81 ± 0.073	45.89 ± 0.42	6.51 ± 0.062	

Table 4
ENF test specimen dimensions (corresponding to Fig. 5b).

Shim thickness (mm)	Length, L (mm)	Width, b (mm)	Bond-line Thickness, t (mm) (Avg ± STV)	Pre-Crack Shim length, a_0 (mm) (Avg ± STV)	Total Sample Thickness, 2 h (mm) (Avg ± STV)	Average Surface Roughness (µm) (Avg ± STV)
0.25	75	25	0.30 ± 0.046	51.41 ± 0.26	6.15 ± 0.18	0.76 ± 0.047
0.48			0.61 ± 0.027	52.68 ± 0.55	6.43 ± 0.088	
0.63			0.72 ± 0.069	52.46 ± 0.36	6.48 ± 0.070	

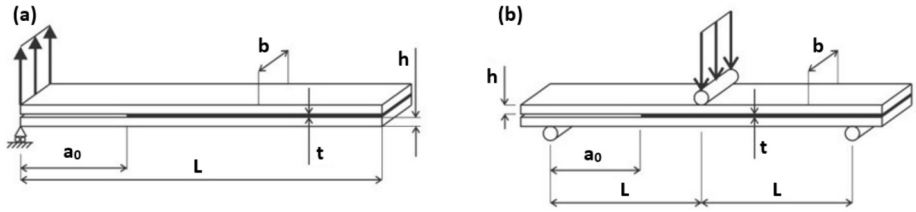

Fig. 5. A) dcb, and b) enf specimen schematics ([] adapted from Ref. 59).

3. Experimental setup and data reduction

3.1. Experimental setups

An MTS 810 servo-hydraulic test frame with a ± 50 kN capacity load cell (signal variability ± 100 N) was used to perform all DCB and ENF tests. Mechanical wedge grips were used for the DCB tests (Fig. 6), while an adjustable three-point bending test fixture with a support span set to 150 mm was used for the ENF tests (Fig. 7). Note, an alignment bracket was used to center the ENF specimens and position them parallel with the edge of the fixture. All tests were performed in displacement control with a constant displacement rate of 0.1 mm/s. Load and displacement data was captured at a frequency of 2 Hz for the RT DCB and ENF tests, which was sufficient due to the high ductility of the adhesive (discussed in Section 4). Due to the brittleness of the material response at LT (see Section 4), the load and displacement data was captured at a frequency of 30 Hz for all LT tests.

The ambient temperature for all RT tests was recorded as 23 °C. To perform the LT tests (–40 °C), the test frame was equipped with an Instron 3119–609 liquid nitrogen-cooled climate chamber. Once the specimens were gripped or aligned, the chamber was cooled at

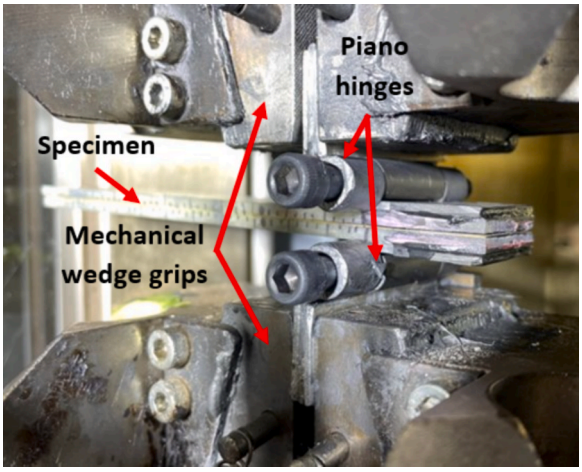

Fig. 6. Image of a DCB specimen gripped from the loading hinges. The loading hinges were aligned within the grips prior to tightening to avoid specimen preloading.

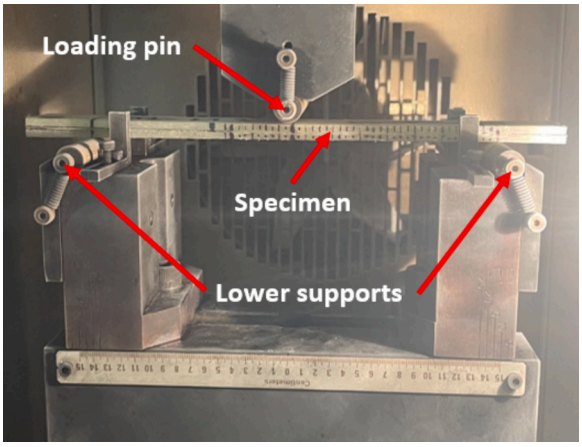

Fig. 7. Image of an ENF specimen mounted on the three point bend fixture. The specimens were aligned such that the midspan coincided with the central loading pin.

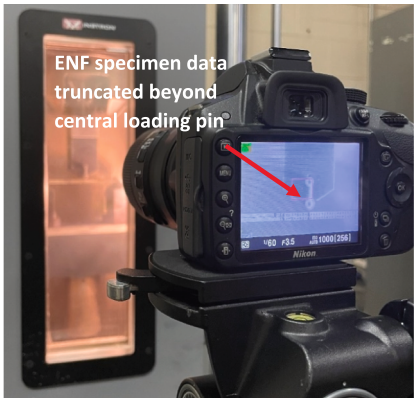

Fig. 8. Image of a low temperature ENF test with the DSLR camera observing through the heated chamber window.

a rate of –6.3 °C/min, reaching the test temperature of −40 °C in 10 min. Once the test temperature was attained, the specimens were allowed to reach thermal equilibrium during a 5 min interval (confirmed using a surface mounted thermocouple). The test frame was set to load control during the temperature cooldown to allow for unrestricted contraction under zero load, thus avoiding preloading of the specimen during the temperature cooldown. The climate chamber comprised a heated observation window that prevented frosting during LT tests, which enabled unrestricted observation of the specimens during the tests (Fig. 8).

A Nikon D3200 DSLR camera with a Sigma EX 180 mm lens was used to track the propagation of the crack tip in the adhesive layer. The camera tracked the relative displacement of discrete markers that were evenly spaced at 2.5 mm increments ahead of the initial crack tip (Fig. 10). Video of the adhesive deformation was captured with a resolution of 1920 x 1080 pixels at 30 FPS. The load–displacement data was synchronized with the DSLR camera footage.

3.2. Data reduction schemes

Two separate data reduction schemes were used to compute the Mode I strain energy release rate (SERR), G_I, corresponding to crack initiation and propagation. The Simple Beam Theory (SBT) method was used to compute the critical SERR, G_{IC}, at crack initiation [60], while the Modified Beam Theory (MBT) method was used to compute G_{IC} corresponding to crack propagation. The MBT method is a commonly employed data reduction scheme for computing the SERR, G_I, as indicated in the standard ASTM D5528 [22]. Gálvez et al. [61] demonstrated that the MBT method can be used reliably in conjunction with DSLR footage for a ductile thermoplastic adhesive, while the method has been used to compute crack propagation fracture energies [60]. The calculation of G_I via the MBT method is given by:

$$G_I = \frac{3P\delta}{2b(a+|\Delta|)} \tag{1}$$

where P is the load, δ is the load line displacement, b is the specimen width, a is the crack length, and Δ is a compliance correction factor. The Δ parameter was computed from the cubed root of the beam compliance (Fig. 9) [54]. The crack length a was determined using DSLR video footage, and post-processed using the Tracker open-source software tool [62]. The software followed discrete marker points positioned at 2.5 mm increments on each of the substrates to determine the precise moment when the markers began vertically separating from each other and, thus, enabling calculation of G_I propagation. A graphical explanation for this solution at one discrete marker increment is shown in Fig. 10 [54]. An image of a DCB specimen during a test shows the development of the fracture process zone (FPZ) in the adhesive near the indicated discrete points, which is indicated by whitening ahead of the crack tip (Fig. 10a). Whitening during testing was caused by light scattering due to progressive cavitation and deformation (manifested as crazing and shear banding) of the ductile MMA adhesive system during mechanical loading The onset of whitening occurred at the same instant that the software identified the relative movement of the indicated markers. The visually inspected SERR values were within 1 % of values recorded using discrete markers, demonstrating the degree of ductility within the MMA adhesive. Once the crack tip locations were synchronized with the load–displacement curve, the MBT method was used to determine G_I at each discrete points for the corresponding crack length (i.e., R-curve). By averaging the discrete G_I values, the G_{IC} for crack propagation was computed for the adhesive system for a given bond-line thickness.

Owing to issues with observing the crack tip during stick–slip propagation, the Δ calibration parameter from the MBT method could not be adopted for LT DCB tests. Such problems with data reduction at LT conditions have been previously reported [36,63]. Thus, the SBT method was adopted for all G_{IC} initiation calculations. While the SBT method may underpredict SERR compared to the MBT method [60], the SBT method is still feasible as a comparison tool between G_{IC} initiation at RT and LT conditions. In the fracture initiation analysis, the peak force was assumed to coincide with the initial crack length measured via microscope. The calculation of G_I via the SBT method is given by:

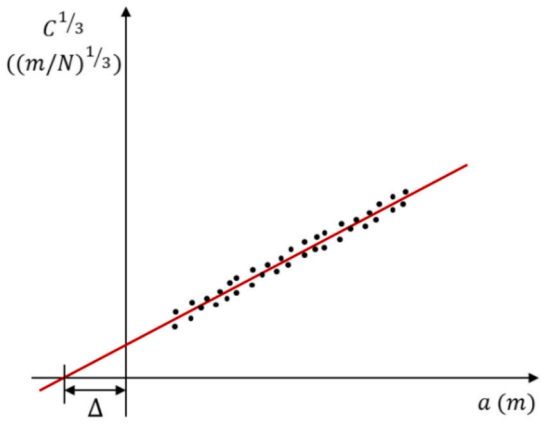

Fig. 9. Schematic showing calculation of Δ calibration parameter for the Modified Beam Theory [54].

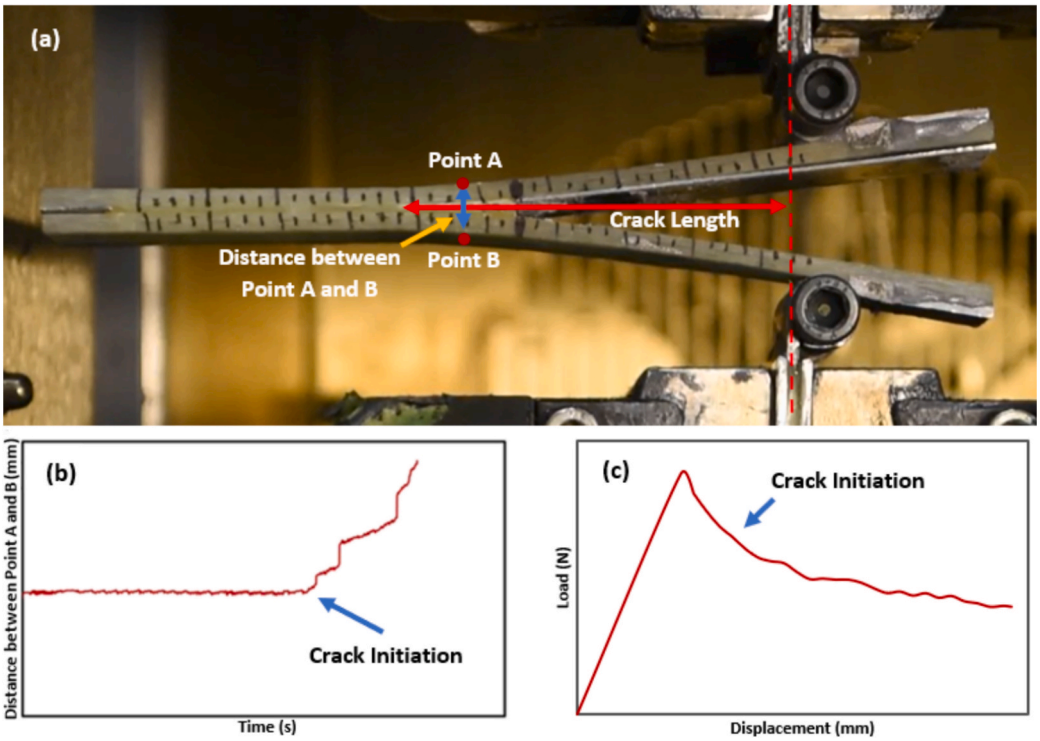

Fig. 10. Demonstration of crack tip monitoring scheme for a discrete marker increment: (a) image of DCB specimen showing markings that were tracked using the DSLR camera, (b) sample point distance versus time plot indicating instant that Points A and B begin to separate as a result of the propagating crack tip, and (c) sample load–displacement plot indicating instant that crack tip reaches Points A and B. Schematics plots [] adapted from 54.

$$G_I = \frac{4P^2}{E_s b^2} \bullet m \tag{2}$$

where the dimensional variables follow the MBT method, E_s is the tensile modulus as given in Table 1, and m is the following:

$$m = \frac{3a^2}{P^2} + \frac{1}{h} \tag{3}$$

Although crack tip monitoring was feasible for DCB tests to enable calculation of G_{IC}, there has not been a widely accepted crack tip monitoring solution for Mode II ENF tests. In this study, the crack tip was not clearly discernible during the ENF tests as shown in Fig. 11, where "intermittent whitening" adversely influenced the confidence in accurate crack tip identification. Additionally, the bending of the substrates during ENF testing did not allow the Tracker software to be used effectively, since the corresponding marker points slid in multiple axes relative to each other. Issues with observing the crack tip affected both initiation (due to difficulties correlating video footage with the Load-Displacement curves during RT conditions) and propagation crack resistance calculations. Data reduction schemes exist in the literature – such as the Compliance-Based Beam Method (CBBM) – that utilize an artificial (or effective) crack tip computation, where the material properties of the substrate are used to determine G_{IIC} instead of crack tip monitoring [64]. However, this method was not considered for either G_{IC} or G_{IIC} in this study.

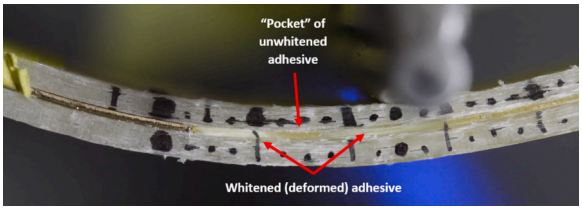

Fig. 11. Crack tip identification during Mode-II adhesive failure was not reliably feasible preventing calculations of G_{IIC}. Figure demonstrates intermittent whitening that prevented a definitive metric for locating the crack tip.

4. Results and discussion

4.1. DCB tests (Mode I)

For each condition, three specimens were tested and the load–displacement response for repeated tests corresponded well with minimal variability up to the peak load (see initial stiffness and peak load in Table 5 and Table 6), beyond which slightly greater variability was observed (Fig. 12). The RT DCB load–displacement response was characterized by an initial linear region up to the peak load followed by a gradual decrease in load, which is indicative of stable crack propagation. On the other hand, the LT DCB specimens were characterized by a sudden sharp drop in load after the initial linear region due to the occurrence of unstable crack propagation, owing in part to the increased brittleness of the adhesive at low ambient temperature. The associated post-peak response was characterized by load jumps and drops, signifying unstable stick–slip crack propagation as the elastic energy was gradually absorbed by the adhesive layer until reaching a threshold value that repeated the stick–slip cycle [36,48]. At any given bond-line thickness, the initial stiffness of the LT DCB specimen was greater than the RT DCB specimen (e.g., 55 % higher for a bond-line thickness of 0.25 mm), while the peak force for the former was less than that of the latter (e.g., 20 % lower for a bond-line thickness of 0.25 mm). The increased brittleness of the adhesive at LT coupled with the residual stresses that developed in the adhesive during thermal cooldown owing to the mismatch in CTE between the adhesive and adherends (see Appendix and Section 4.3) may have decreased the ability of the adhesive to sustain load at LT. An increased variability in the response was observed for the LT DCB specimens, particularly the post-peak response as indicated by the displacement at failure (Table 5 and Table 6), which is further indicative of the existence of residual stresses in the adhesive. The influence of thermal residual stresses in adhesive joints on the Mode I fracture toughness and failure behaviour have been previously reported for other adhesively bonded joints [28,29,30,31,65].

The performance of the MMA adhesive was also dependent on the bond-line thickness. For the RT DCB specimens, the average peak force increased by 17 % with increasing bond-line thickness over the range considered. Similar results were also reported previously for epoxy-based adhesives under RT conditions [21], where an increase in bond-line thickness corresponded to an increase in peak force. This characteristic is a result of the decrease in the constraining effect on the adhesive caused by the adherends at higher bond-line thicknesses, which generally promotes greater adhesive plastic deformation and higher joint performance [66]. Kinloch and Shaw [67] have reported that the plastic zone ahead of the crack tip in an adhesive will fully develop at higher bond-line thicknesses resulting in greater joint performance (G_{IC}) up to a certain threshold, beyond which the joint performance begins to decrease. Moreover, the initial stiffness of the RT DCB specimens decreased by 24 % with increasing bond-line thickness, which was not a surprising result. The LT-DCB specimens similarly exhibited a 26 % decrease in initial stiffness with increasing bond-line thickness over the same range. However, in contrast, under LT conditions the peak force decreased by 32 % with increasing bond-line thickness over the range considered, which is analogous to the results reported by Jia et al. [48] for a polyurethane adhesive but contrary to the results reported by Rahmani and N. Choupani [31] for an epoxy adhesive. It is plausible for the tested DCB specimens that at low ambient temperature the bond-line thickness threshold was lower than that at RT and was exceeded for the thinnest bond-line thickness. Thus, according to Kinloch and Shaw [67], this could be contributing to the observed decrease in the associated peak force with increasing bond-line thickness at LT.

The average R-curves for the RT DCB specimens reveal a slight decrease in SERR with increasing crack length (Fig. 13). Such fracture behaviour has been previously reported in the literature for MMA adhesives [27,52] and polyurethane adhesives [61]. Fernandes et al. found that while R-curves may demonstrate a plateau at a certain bond-line thickness, increasing the bond-line thickness gradually yields a falling R-curve as the crack progresses [66]. The decline in SERR with crack length is greatest in the 0.25 mm bond-line thickness samples; referencing analysis from Arenas [39], this may suggest a localized transition to adhesive failure from bulk cohesive behaviour. Towards higher bond-line thicknesses, Castagnetti [46] observed incomplete polymerization in MMA adhesives at increased bond-line thicknesses which could point towards similar localized imperfections explaining the phenomenon rather than systematic errors in the analysis. While Campilho et al. [68] and Saleh et al. [69] have highlighted some caution with applying LEFM techniques to ductile adhesive, the compliance factor incorporated in the MBT method should broadly correct for such behaviour even accounting for discrepancies caused by errors in observing the *apparent* crack length and the mechanical *effective* crack length.

At RT, the average initiation G_{IC} values peaked for specimens with a bond-line thickness of 0.635 mm, with a value 18 % higher than specimens with 0.25 mm bond-line thickness (Table 7). While the average initiation G_{IC} values decreased by 7 % for specimens with a 0.8 mm bond-line thickness when compared to those with a 0.635 mm thickness, there was notable scatter in the values for the former specimen (Table 7). Furthermore, the propagation G_{IC} values for the RT DCB specimens increased by 82 % over the range of bond line thicknesses considered (Table 8), where the crack propagation speed was insensitive to the bond-line thickness (see crack

Table 5
Average peak force, initial elastic stiffness, and displacement at failure for RT-DCB specimens with standard deviation. P-value from one-way ANOVA analysis shown in bottom row for each parameter.

Bond-line Thickness (mm)	Initial Stiffness (N/mm)	Peak Force (N)	Displacement at Failure (mm)
0.25	21.1 ± 1.0	142.4 ± 6.1	22.2 ± 1.7
0.635	20.2 ± 0.5	161.8 ± 3.3	32.7 ± 1.0
0.8	16.6 ± 1.0	166.0 ± 5.6	31.8 ± 2.2
P-value	0.010	0.017	0.0048

Table 6
Average peak force, initial elastic stiffness, and displacement at failure for LT-DCB specimens with standard deviation.

Bond-line Thickness (mm)	Initial Stiffness (N/mm)	Peak Force (N)	Displacement at Failure (mm)
0.25	32.8 ± 3.4	113.4 ± 8.3	13.4 ± 2.5
0.635	24.4 ± 3.1	94.5 ± 5.5	10.9 ± 2.6
0.8	24.5 ± 2.8	76.6 ± 1.3	9.30 ± 0.9
P-value	0.055	0.0021	0.23

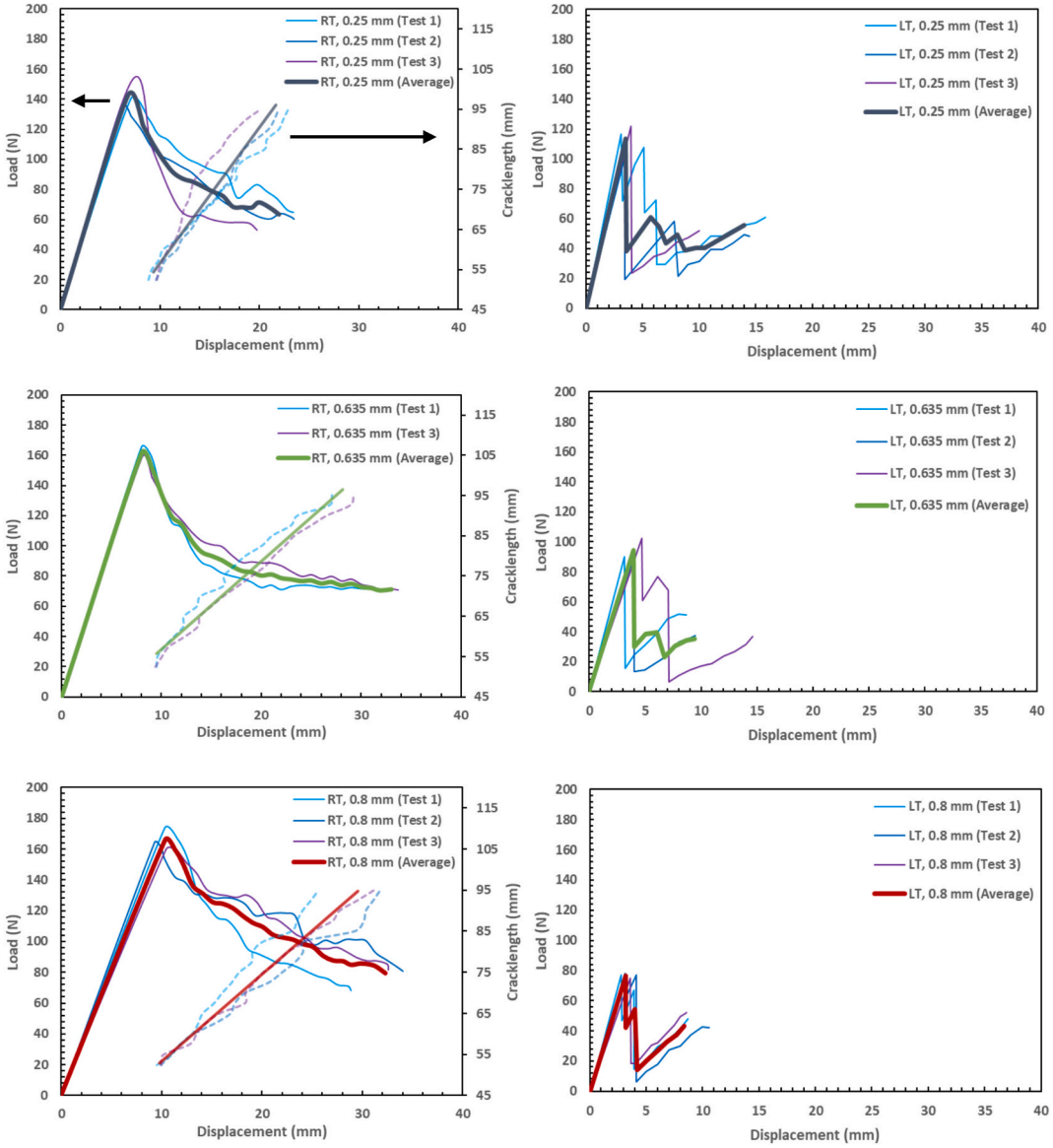

Fig. 12. Load-displacement responses for specimens with distinct bond-line thicknesses: (a), (c), (e) RT DCB specimens, and (b), (d), (f) LT DCB specimens. Specimen bond-line thickness specified in plot legends in units of mm.

length-displacement data in Fig. 12). The increasing trend of initiation and propagation G_{IC} values with increasing bond-line thickness under RT conditions corresponds to the associated increase in peak force. In contrast, at LT the initiation G_{IC} values decreased by 60 % with increasing bond-line thickness over the range considered (Table 7), which also corresponds to the associated decrease in peak force described previously. Furthermore, for specimens with a 0.8 mm bond-line thickness, the average initiation G_{IC} decreased by 77 % under low ambient temperatures when compared to RT conditions, further revealing the negative correlation between crack

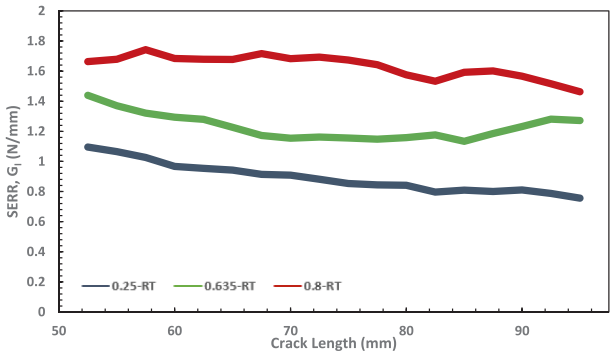

Fig. 13. Average R-curves for RT DCB specimens using MBT method. Bond-line thickness indicated in units of mm.

Table 7
Average initiation G_{IC} for RT and LT DCB specimens with standard deviation.

Bond-line Thickness (mm)	RT Initiation G_{IC} (N/mm)	LT Initiation G_{IC} (N/mm)
0.25	0.99 ± 0.07	0.610 ± 0.09
0.635	1.16 ± 0.05	0.389 ± 0.05
0.8	1.08 ± 0.1	0.244 ± 0.01
P-value	0.40	0.0020

Table 8
Average propagation G_{IC} for RT DCB specimens with standard deviation.

Bond-line Thickness (mm)	Propagation G_{IC} (N/mm)
0.25	0.892 ± 0.1
0.635	1.23 ± 0.07
0.8	1.63 ± 0.1
P-value	0.0042

resistance and temperature. Owing to rapid and unstable crack propagation, the MBT method could not be used to establish R-curves for the LT DCB specimens. Such difficulties with data reduction at low temperature have been reported previously [36]. A comparison of the fracture process zones (FPZ) for RT and LT DCB specimens is shown in Fig. 14. While the RT DCB specimens demonstrated notable whitening during adhesive deformation (≈ 7.5 mm long FPZ) which aided with identifying crack tip propagation, no discernible FPZ was observed for the LT DCB specimens.

Sekiguchi et al. [70] and Banea et al. [44] suggested that G_{IC} in ductile adhesives exhibits a positive linear correlation with adhesive thickness until a threshold thickness where G_{IC} gradually begins to saturate. They assumed an argument postulated by Pardoen et al. [71] that proposed an additive partitioning of fracture energy into two components: (1) the intrinsic work of fracture within the cohesive zone G_0, and (2) additional contributions to the adhesive fracture toughness from plastic dissipation and stored elastic energy, G_p, such that $G_{IC} = G_0 + G_p$. Within this framework, G_0 was independent of adhesive thickness, while thickness effects are contained within G_p, and thus increasing fracture energy with increasing adhesive thickness is predominantly caused by plastic dissipation within

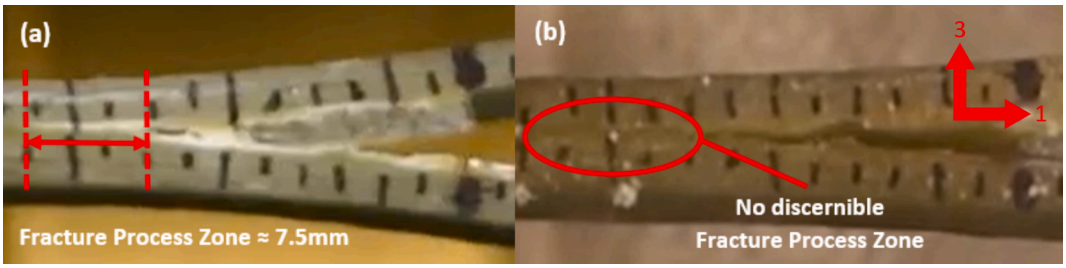

Fig. 14. Comparison between fracture process zones for (a) RT DCB and (b) LT DCB tests with 0.8 mm bond-line thicknesses.

the adhesive layer. Practically, such a relation is a linear equation with a non-zero G_{IC} at zero thickness (since G_p must be zero at zero adhesive thickness). A similar analysis was applied to the G_{IC} propagation values for the RT DCB specimens herein (Fig. 15).

From the linear fit, the values for G_0 and G_p were extracted as 0.54 N/mm and 1.26 N/mm, respectively. From this perspective, it appears that the intrinsic work of fracture is lower than the values reported by Sekiguchi et al. [70] for an MMA adhesive and that the plastic dissipation increases more gradually with bond-line thickness. Results from Banea et al. [44] for a polyurethane adhesive (G_{IC} threshold) yield a similar G_p as Sekiguchi et al. [70], although both studies investigated steel substrates. Adherend stiffness can have a significant influence on the plastic zone constraining effects within the adhesive layer; the Dundurs parameter β captures such near-crack tip oscillatory behavior [43]. It should be noted that within this analysis, unstable crack propagation (i.e, the behavior demonstrated by the LT DCB specimens) would involve minimal plastic deformation, and the intrinsic work of fracture that is independent of adhesive thickness gradually dominates [70].

4.2. ENF tests (Mode II)

For each condition, three specimens were tested and the load–displacement response for repeated tests corresponded well with minimal variability for the duration of the test (Fig. 16, Table 9, Table 10). One of the RT samples with a 0.625 mm thick bond-line experienced a sudden change in elastic stiffness and premature failure due to misalignment during the bonding process and, thus, was not included. The RT ENF specimens exhibited a linear force–displacement response during the early stages of loading followed by a nonlinear response up to the peak load, beyond which the load began to plateau. Note, the RT results were truncated to 25 mm of load-line displacement to ensure that only data recorded prior to the crack tip surpassing the central loading pin is shown (Fig. 8). This response is similar to that reported for a ductile adhesive [50] and is characteristic of stable crack propagation. Conversely, the load–displacement response for the LT ENF specimens was linear up to the peak load, followed by rapid crack propagation and abrupt failure for all bond-line thicknesses. Similar to the Mode I tests, for any given bond-line thickness the ENF specimens sustained a lower peak load at LT when compared to RT (e.g., 39 % reduction for specimens with 0.25 mm bond-line thickness), while the initial stiffness was greater for LT specimens (e.g., 26 % increase for specimens with 0.625 mm bond-line thickness). The former result contrasts with the results reported by Rahmani and Choupani [31] for an epoxy adhesive and Jia et al. [50] for a ductile adhesive where peak force and fracture toughness increased with decreasing temperatures (with the caveat that fracture toughness values were not calculated in this study). The increased brittleness of the adhesive at LT coupled with the thermally-induced residual stresses (see Appendix and Section 4.4) may have contributed to the lower recorded loads during DCB testing at LT for the MMA adhesive considered in this study.

For the RT ENF specimens, the average peak load increased by 13 % with increasing bond-line thickness over the range considered, which is analogous to the Mode I results. However, the initial stiffness was consistent across all bond-line thicknesses for both the RT ENF and LT ENF specimens. Conversely, the average peak force for the LT ENF specimens did not exhibit a clear trend with bond-line thickness. The peak force for the two thinner bond lines were statistically equivalent, whereas for the largest bond-line thickness (0.625 mm) the average peak force was lower but the standard deviation was irregularly large (20 % of the average).

A comparison of the FPZ for the RT and LT ENF specimens reveals a markedly distinct phenomenon. For the RT ENF specimens, the adhesive undergoes significant whitening (Fig. 17a), albeit nonuniformly which hindered the ability to use whitening as an optical trigger for crack-tip tracking. Conversely, for the LT ENF specimens significantly less whitening was observed when compared to the RT ENF specimens, while the crack path followed the adherend-adhesive interface (Fig. 17b), which will be further illuminated via fractographic analysis (Section 4.4).

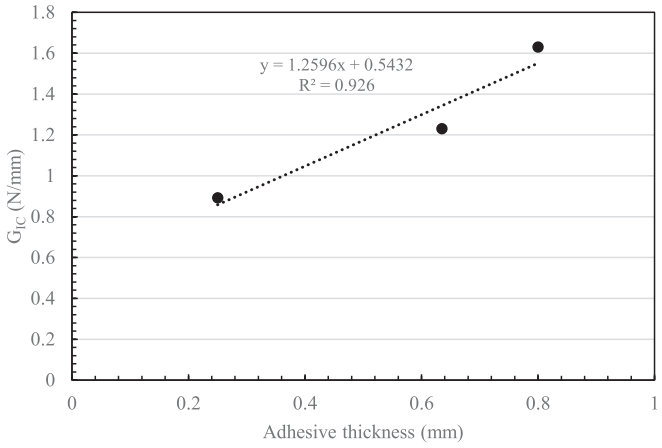

Fig. 15. Propagation G_{IC} plotted against adhesive thickness with linear fit for RT DCB specimens to express fracture energy as additive partitioning of two components.

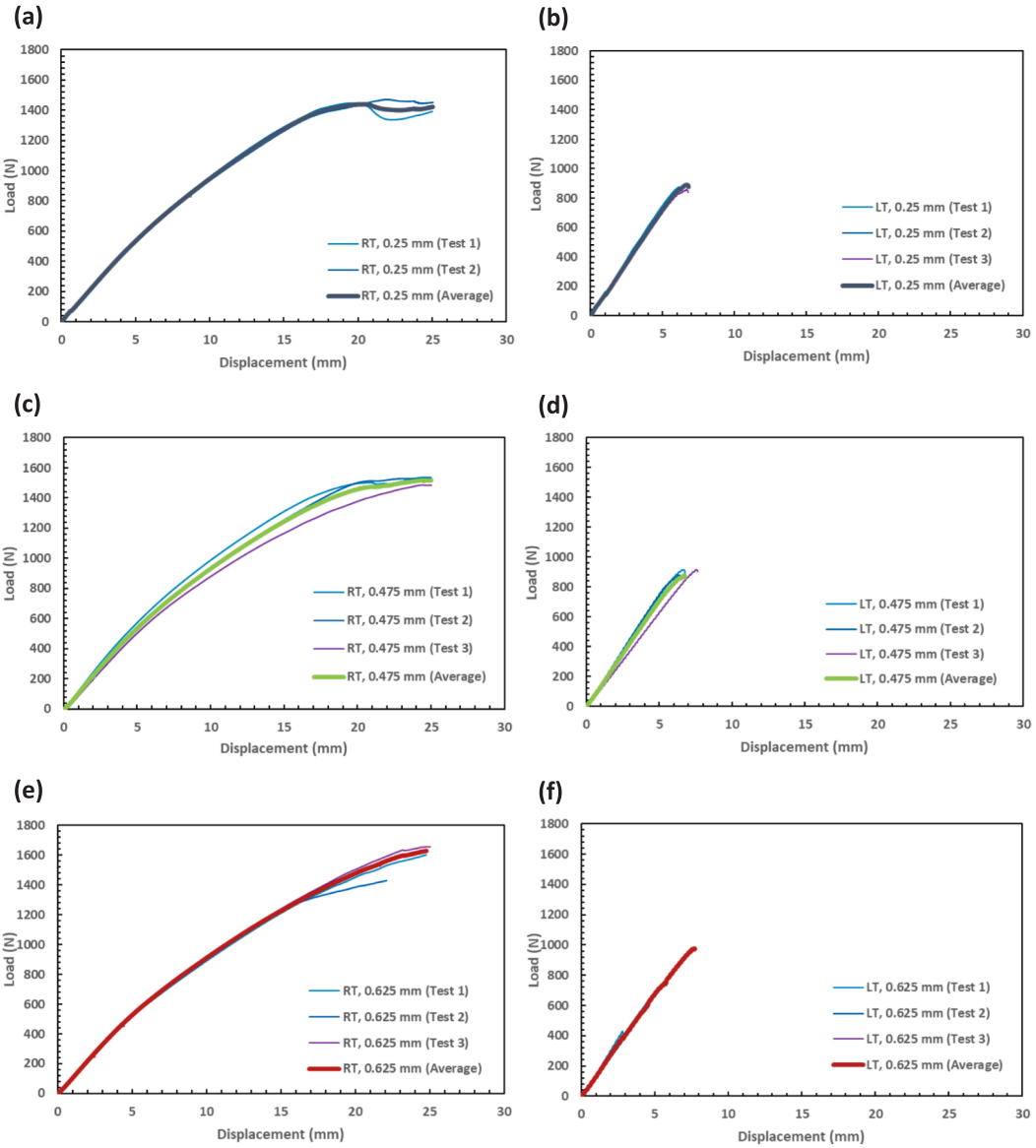

Fig. 16. Load-displacement responses for specimens with distinct bond-line thicknesses: (a), (c), (e) RT ENF specimens, and (b), (d), (f) LT ENF specimens. Specimen bond-line thickness specified in plot legends in units of mm.

Table 9
Average peak force and initial elastic stiffness for RT ENF specimens with standard deviation.

Bond-line Thickness (mm)	Initial Elastic Stiffness (N/mm)	Peak Force (N)
0.25	108.9 ± 1.6	1459.7 ± 12.1
0.475	111.2 ± 9.4	1518.5 ± 22.9
0.625	108.9 ± 2.0	1630.2 ± 27.0
P-value	0.92	0.0098

4.3. DCB specimen fracture surface analysis

Fractography of the RT DCB specimens revealed cohesive failure for all bond-line thicknesses. The adhesive failed in a highly ductile manner and was characterized by a large FPZ, akin to previously reported Mode I failure modes for MMA adhesives at RT [25,27,52]. The whitened fracture surface caused by the FPZ was broadly uniform throughout the adhesive layer (Fig. 18). Widespread

Table 10
Average peak force and initial elastic stiffness for LT ENF specimens with standard deviation.

Bond-line Thickness (mm)	Initial Elastic Stiffness (N/mm)	Peak Force (N)
0.25	141.7 ± 6.9	876.1 ± 12.0
0.475	140.4 ± 13.4	904.6 ± 17.0
0.625	137.5 ± 9.6	770.4 ± 159.5
P-value	0.92	0.38

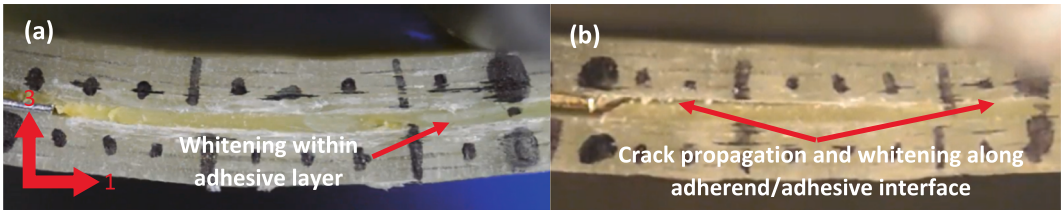

Fig. 17. Comparison between fracture process zones for (a) RT ENF and (b) LT ENF tests with 0.625 mm bond-line thicknesses.

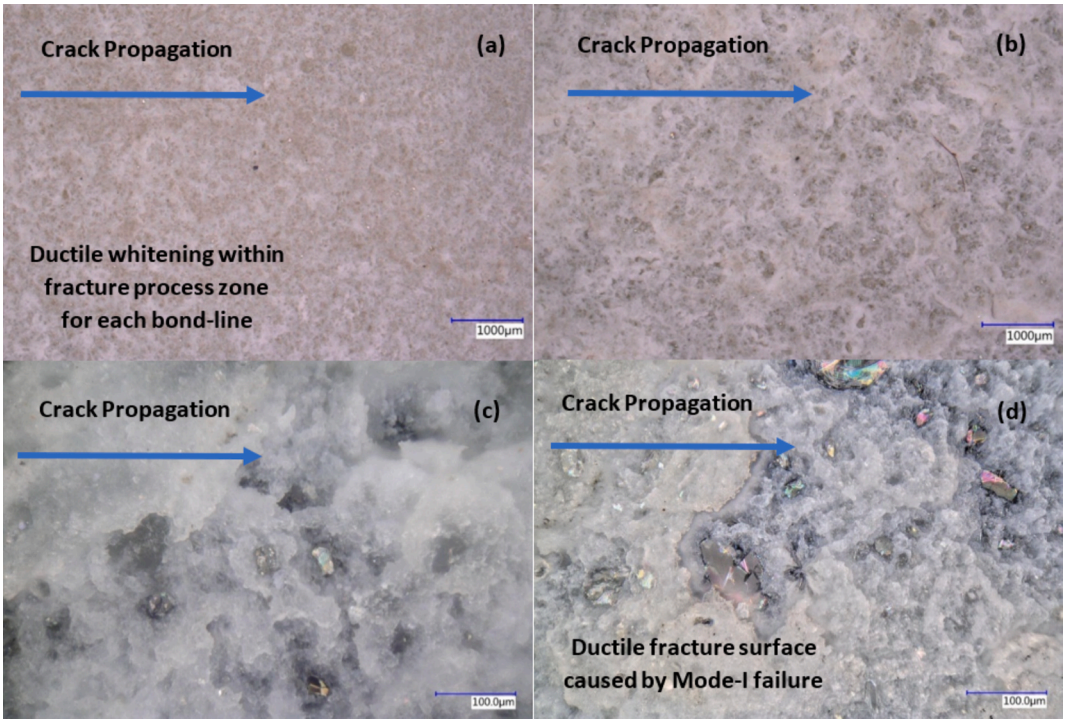

Fig. 18. Fracture surfaces of RT DCB specimens revealing whitening due to ductile deformation. Low magnification images of specimens with bond line thicknesses of: (a) 0.25 mm, and (b) 0.8 mm. High magnification images of the same specimens with bond line thicknesses of: (c) 0.25 mm, and (d) 0.8 mm.

ductile adhesive failure resulted in a gradual decrease in the post-peak load (Fig. 12) and the observed stable crack propagation.

The fractured surfaces of the LT DCB specimens were visually distinct from the RT specimens. Unlike the whitened, ductile fracture surface for the RT specimens, the LT specimens were smooth in appearance (Fig. 19a) which was indicative of brittle fracture. Distinct, wave-like crack fronts that oscillated between substrates were observed for certain specimens (Fig. 19b). These oscillatory fracture surfaces contained adhesive peaks and ridges that were each between 2 – 5 mm in length (see schematic in Fig. 19c). Furthermore, the adhesive ridges contained exposed stitching implying that the crack front propagated slightly into the substrate itself. Despite the reduced load capacity of the specimens at LT (Table 6), the substrate damage indicated that the bond strength was not the cause of failure. Transitory failure modes that are dependent on the ambient temperature have been captured via fractographic analysis for polyurethane adhesives [51], epoxy adhesives [31,72], and thermoplastic composite joints [36].

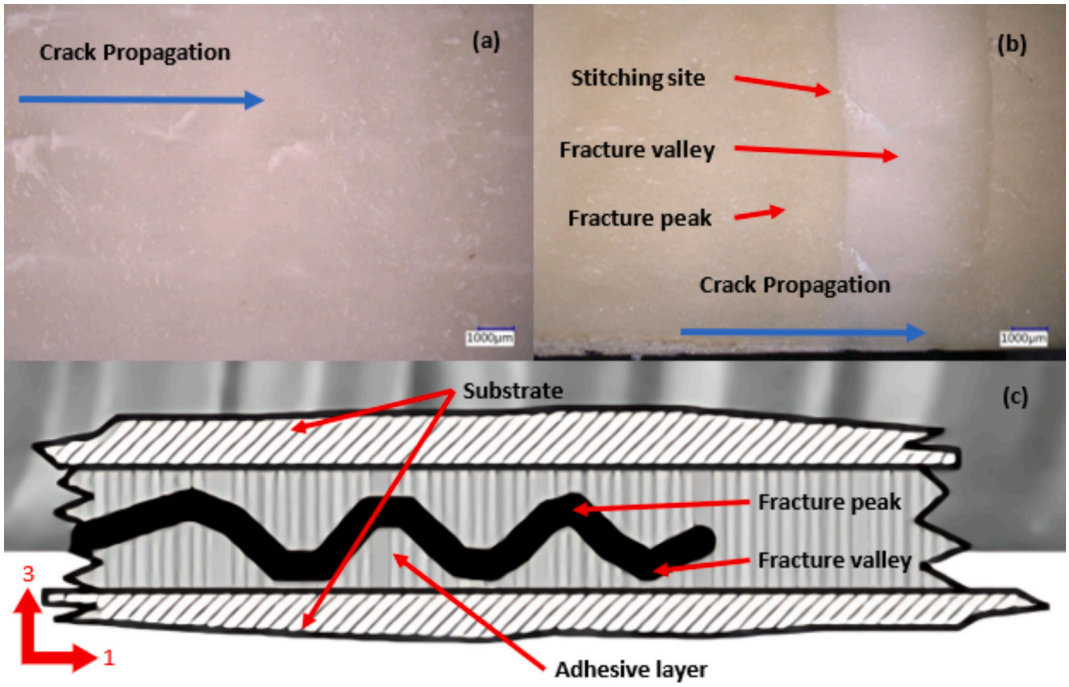

Fig. 19. Fracture surfaces of LT DCB specimens with bond line thicknesses of: (a) 0.25 mm, and (b) 0.8 mm. (c) schematic of oscillatory crack propagation.

The oscillatory crack tip propagation patterns were investigated in further detail using a 3D depth display feature on the opto-digital microscope that generated a contour plot of the fracture surfaces and quantified the amplitude of the oscillations. The depth of the oscillations for each specimen was equal to the corresponding bond-line thickness (Fig. 20), confirming that the crack front oscillated between substrate surfaces. It is clear that the dominant failure mode for the adhesive was cohesive as the crack tip propagated through the thickness of the adhesive layer itself. Chen et al. [73] observed oscillatory crack propagation in the adhesive layer of DCB specimens and investigated the effect of residual stress (and subsequently the local stress component at the crack tip acting parallel to the crack plane, i.e., the T-stress) on crack stability. The oscillation frequency was correlated with the degree of residual stress sustained during preliminary tensile loading, prior to the DCB test. Thus, it can be inferred that the difference in thermal expansion coefficient values between the substrate and the adhesive induced a residual stress in the specimens during the temperature cooldown, which contributed to the crack tip instability. Specifically, the adhesive layer is expected to contract more rapidly with decreasing temperature than the adherend resulting in tensile stresses at the interfacial layer [36]. The influence of the T-stress on the tensile fracture energy of brittle adhesives was also investigated by Akhavan-Safar et al. [74], where a large effect of the bond-line thickness on G_{IC} as a result of the T-stress was reported. Finite element simulation models of the DCB specimens with different bond-line thicknesses were developed to quantify the residual stresses during thermal cooldown (see Appendix). For all DCB specimens, the peak residual stress in the adhesive layer reached a value that was approximately 50 % of the ultimate tensile strength of the MMA adhesive, which supports the fact that residual stress contributed to the unstable crack oscillation observed. The 3D depth display was also used to assess the fracture surface of the RT specimens with the thickest bond line, and it was observed that the Rz topographic variance was less than 200 µm (Fig. 21).

Fernandes et al. [75] observed peaks and valleys via fractographic microscopy with an additional ATR-FTIR analysis helping to conclude that near-interface failures were cohesive rather than adhesive. The variation in the failure locus was considered in a subsequent study via the T-stress instability [76]; the constraining effects of the adherend were relaxed at thicker bond-lines [43]. Yoshimura et al. [63] also observed oscillatory crack tip propagation where cryogenic conditions caused catastrophic crack tip advance that prevented accurate measurements of fracture toughness.

To verify that the adhesive failed completely in a cohesive manner, high magnification microscopic analysis was conducted on the fracture peaks and ridges of the tested LT DCB specimens (Fig. 22). The high magnification analysis confirmed that – independent of the underlying thickness of the adhesive region – the fracture surface maintained a consistent appearance. The adhesive fracture surface was also compared with the un-bonded substrate surface at high magnification to ensure that the failure mode was not interfacial. While the LT fracture surface was smoother than the ductile cohesive failure observed on the fracture surfaces of the RT specimens, the un-bonded surface was still smoother by comparison. A pure interface failure would have yielded a clean fracture surface like the un-bonded example [77], but this was not observed under the microscope.

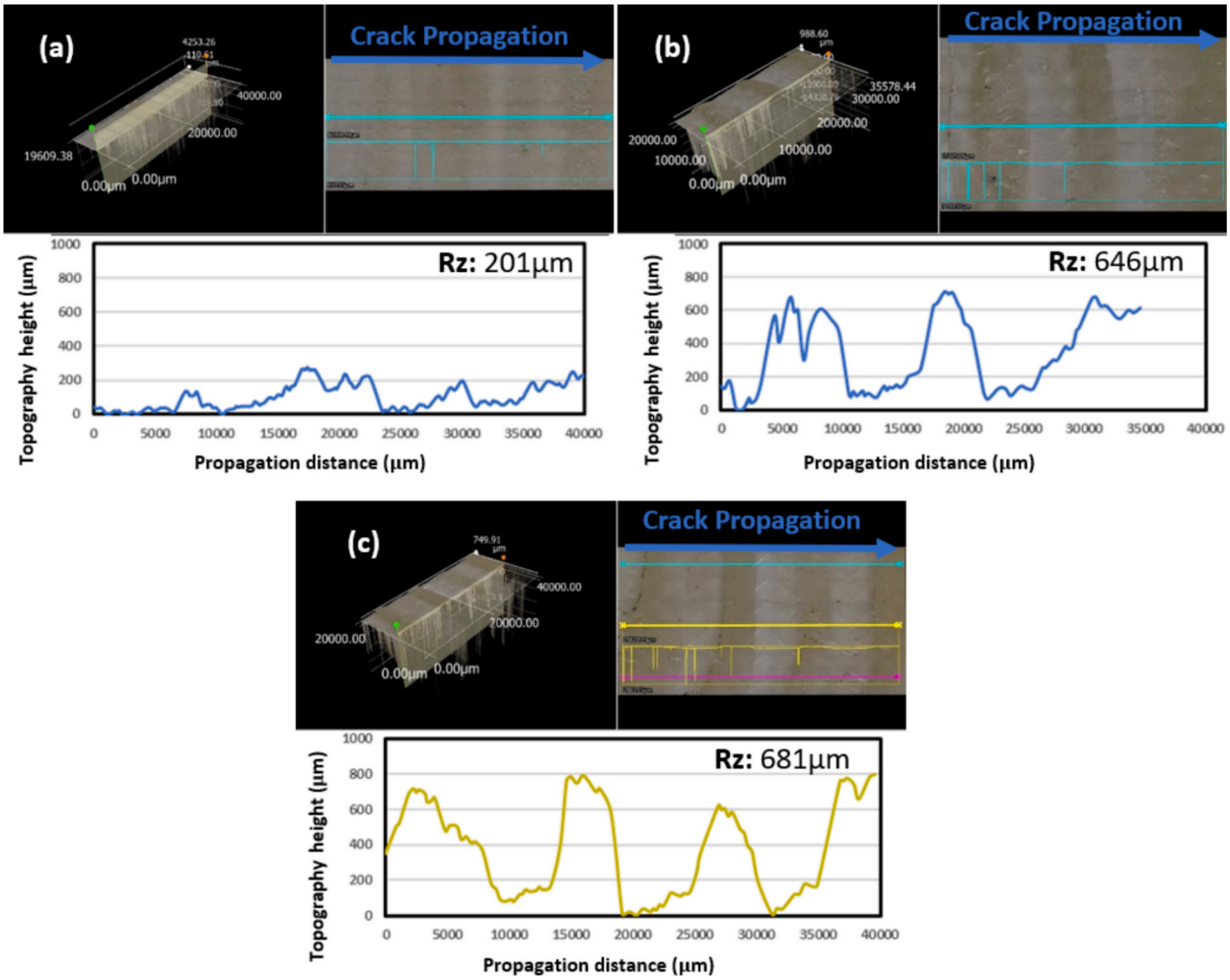

Fig. 20. Results of 3D depth display used to characterize surface roughness for LT DCB specimens with bond line thicknesses of: (a) 0.25 mm, (b) 0.635 mm, and (c) 0.8 mm. The corresponding surface roughness (Rz) is included in each plot.

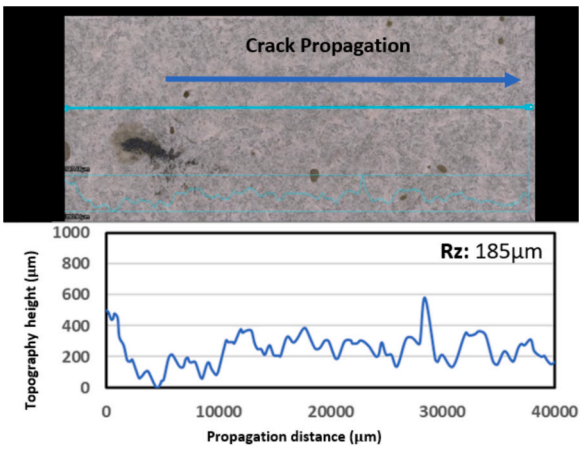

Fig. 21. Results of 3D depth display for a RT DCB specimen with 0.8 mm bond line thickness revealing that the roughness of the fracture surface was uniform.

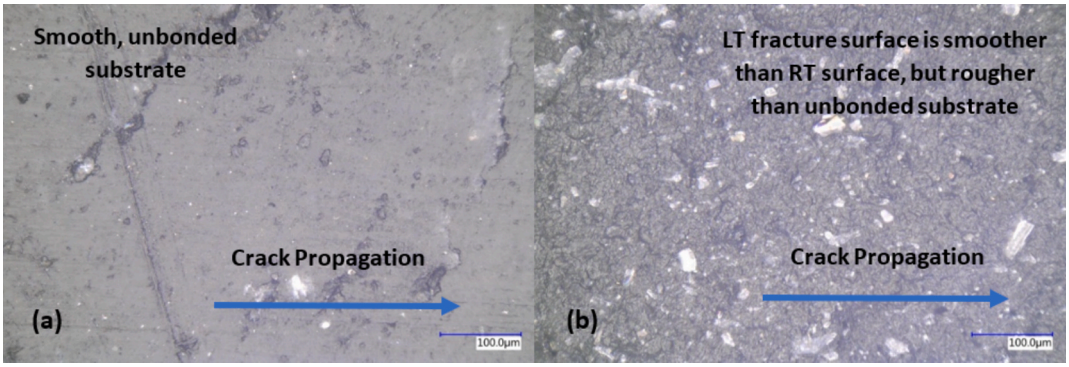

Fig. 22. (a) Image of the surface of a substrate (unbonded, untested). (b) Image of the fracture surface at the valley region for a LT DCB specimen with 0.8 mm bond line thickness. Image magnifications are 500x.

4.4. ENF specimen fracture surface analysis

The fracture surfaces of the RT ENF specimens shared characteristics with those of the RT DCB specimens. A ductile failure mode was evidenced by a whitened fracture surface that formed in the FPZ, and the adhesive failed in a purely cohesive manner with an equal deposit remaining on both substrates. Compared to the RT DCB specimens, the RT ENF specimens had a greater amount of hackle formations in the adhesive layer (Fig. 23), indicating shear failure. The high degree of ductility under shear led to the nonlinear force–displacement response for the RT ENF specimens (Fig. 16). Cohesive failure during quasi-static single lap joint (SLJ) tests at RT conditions have previously been reported [18,24,78], although less attention has been given to pure Mode II failure. The highly whitened deformed adhesive layer has been reported for Mode II failure [31,33], which is consistent with that observed in this study, although unstable crack propagation with adherend failure has also been observed at RT conditions [26].

On the other hand, the LT ENF specimens failed in a brittle manner characterized primarily by fibre-tear failure within the substrate, signifying a transition from cohesive failure at RT to adhesive failure at LT. Previous studies have reported a similar transition in the Mode II failure mode at LT for composite joints bonded with an epoxy adhesive [31,33]. Fractographic analysis showed a large degree of fibre pullout from each specimen irrespective of bond-line thickness (Fig 24a-b), indicating that the adhesive bond was stronger than the substrate itself during LT under shear loading. High magnification fractography for the LT ENF tests confirmed the brittle nature of the failure modes within the substrate. Irrespective of bond-line thickness, the specimens contained either exposed fibres (within the damaged substrate) or fibre imprints (within the adhesive layer that remained attached to the undamaged substrate). The fracture surfaces within the tows contained shear cusps and fibre imprints (Fig 24c-d), further signifying brittle failure. Unlike the LT DCB specimens, the LT ENF specimens did not experience unstable, oscillatory crack tip propagation between the substrates. Nonetheless, the propensity for substrate failure implied that the thermal residual stresses that developed during cooldown (see Appendix) contributed to the transition in the failure mode observed at LT.

5. Conclusions

The study aimed to characterize the Mode I and Mode II fracture response and surface morphology of a unidirectional non-crimp fabric glass fibre-reinforced reactive polymethyl methacrylate (PMMA) composite material bonded with a methyl methacrylate adhesive (MMA) under room temperature (RT) and low temperature (LT; –40 °C) conditions. Double cantilever beam (DCB) and edge

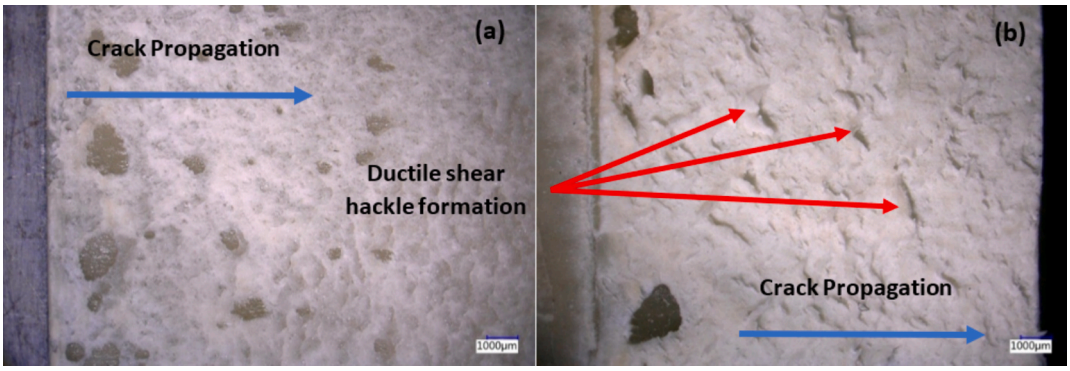

Fig. 23. Fracture surfaces of RT ENF specimens with bond line thicknesses of: (a) 0.25 mm, and (b) 0.625 mm. Images reveal hackle formation due to shear deformation.

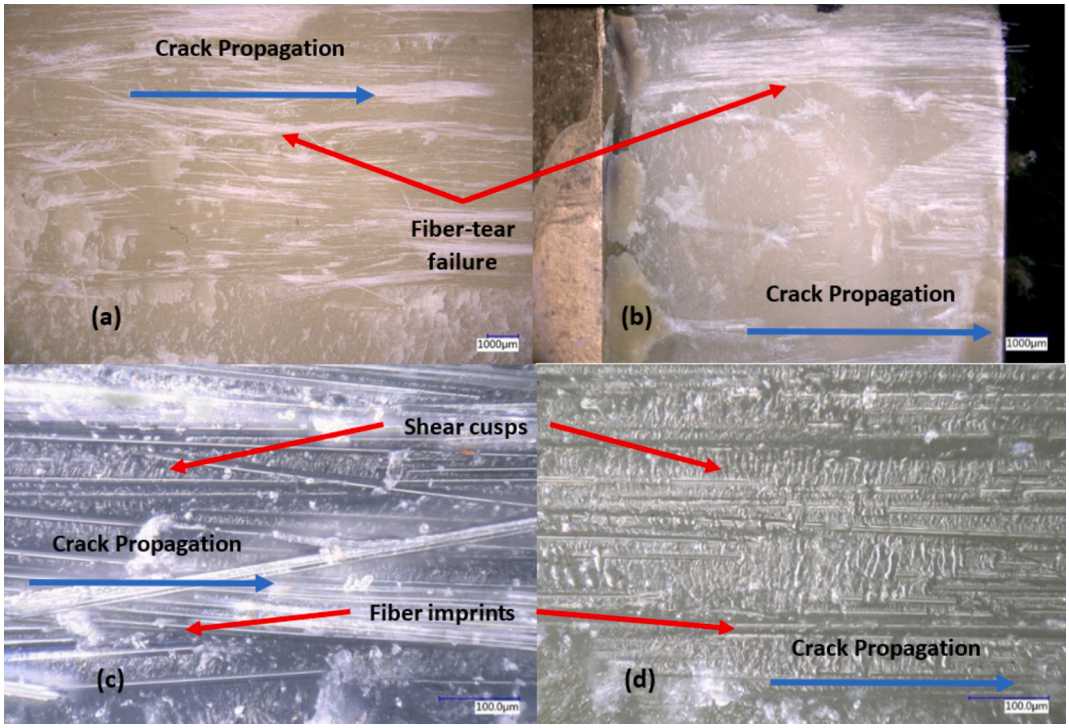

Fig. 24. Fracture surface of LT ENF specimens. Low magnification images of specimens with bond line thicknesses of: (a) 0.25 mm, and (b) 0.625 mm, reveal fibre-tear failure within substrate, while high magnification images (c), (d) show shear cusps and fibre imprints indicative of brittle failure.

notch flexure (ENF) tests were conducted on specimens with three different bond-line thicknesses to quantify the effect of temperature and bond-line thickness on joint performance, while optical microscopy enabled in-depth assessment of the fracture surfaces.

Mode I fracture test revealed that for a given bond-line thickness the peak force and initiation fracture toughness decreased at LT owing to the increased brittleness of the adhesive as well as the residual thermal stresses that developed in the adhesive during temperature cooldown. RT DCB specimens exhibited cohesive failure and stable crack propagation with fracture surfaces characterized by notable ductile deformation and a minor sensitivity to the bond-line thickness. In contrast, LT DCB specimens exhibited sudden unstable oscillatory crack propagation within the adhesive which was characterized by a brittle fracture surface. The LT DCB specimens exhibited a strong sensitivity to the bond-line thickness with initiation fracture toughness decreasing by 60 % with increasing thickness over the range considered.

Mode II fracture tests showed that for a given bond-line thickness the peak force also decreased at LT owing to the increased brittleness of the adhesive coupled with the residual thermal stresses in the adhesive. RT ENF specimens exhibited cohesive failure and stable crack propagation with notable ductile deformation observed on the fracture surfaces. The performance of these specimens notably increased with increasing bond-line thickness. On the other hand, LT ENF specimens underwent rapid crack propagation and abrupt failure with brittle fracture of the substrate, which was characterized by fibre tear and pullout and local shear cusps in the matrix between fibres. These specimens demonstrated less sensitivity to the bond-line thickness. Owing to challenges with tracking the crack tip within the ductile adhesive, fracture toughness values were not established for the ENF specimens. In future work, a robust technique for monitoring propagation of the crack tip for the ENF specimens will be pursued to enable use of the data reduction schemes used in this study for DCB specimens.

Overall, the Mode I and Mode II fracture behaviour of the specimens were greatly influenced by the ambient temperature and revealed a notable sensitivity to the bond-line thickness for Mode I at LT and Mode II at RT. The dependence of performance on both the temperature and bond-line thickness will be considered in the design and numerical analyses of associated adhesive joints, while the outcomes of the study will contribute to optimizing their damage tolerance. The study also revealed that the MMA adhesive bonded well with the thermoplastic composite despite minimal surface pretreatment (i.e., abrasion and degreasing).

CRediT authorship contribution statement

Milos Zivkovic: Writing – original draft, Methodology, Investigation, Formal analysis, Conceptualization. **Erli Shi:** Writing – review & editing, Methodology, Investigation. **Wilfried V. Liebig:** Writing – review & editing, Validation. **John Montesano:** Writing – review & editing, Validation, Supervision, Resources, Project administration, Methodology, Funding acquisition, Conceptualization.

Declaration of competing interest

The authors declare that they have no known competing financial interests or personal relationships that could have appeared to influence the work reported in this paper.

Acknowledgements

This study was funded by the Ontario Center of Innovation (OCI) under grant OCE-VIP 34106 and the Natural Sciences and Engineering Research Council of Canada (NSERC) under grant RGPIN-2022-03724. The second author acknowledges the China Scholarship Council (CSC) for additional funding in the form of a scholarship. The Saertex Group is acknowledged for providing the unidirectional non-crimp fabric used to manufacture the composite substrates, while the authors thank Bostik for providing the MMA adhesive used in this study.

Appendix

Finite element models were developed in the commercial software ABAQUS to simulate the deformation of the DCB and ENF specimens and quantify the associated residual stresses during thermal cooling from 23 °C to −40 °C. The specimen geometry followed that presented in Section 2. The elastic properties of the transversely isotropic substrates were taken as the average values at −50 °C presented in Table 1, while the elastic properties of the isotropic adhesive were taken from the literature (Table 11). The value for the coefficient of thermal expansion (α) for the adhesive was provided by the supplier (Bostik, France). Note, the out-of-plane shear modulus, G_{23}, was calculated using the expression $G_{23} = \frac{E_2}{2(1+\nu_{23})}$, with an approximated $\nu_{23} = 0.26$ computed using rule of mixtures [79]. The coefficients of thermal expansion for the substrate, α_1 and α_2, were calculated using Shapery's equations for unidirectional composites [80] and the constituent properties provided in Table 11. Three finite element models each with a different bond line thickness (Table 3 and Table 4) were considered in accordance with reported dimensions of DCB and ENF specimens.

The substrates and adhesive were meshed using 3D solid elements (C3D8R; 8-node linear brick, reduced integration, hourglass control), which measured 1 mm × 1 mm on the plane of the specimen. Three layers of elements were used through the thickness of the substrate, while one layer of elements was used through the half-thickness of the adhesive. Coincident nodes between substrate and adhesive elements were imposed to represent a strong interfacial bond without failure. A $\Delta T = -63$ °C was applied to the model without dimensional constraints on the joint since the tensile machine was held in force control with a zero load signal during the experimental cooling procedure (Fig. 25).

Table 11
Mechanical properties used for the finite element models of the DCB and ENF specimens.

Mechanical Property (units)	Description	Value
MMA Adhesive		
E (GPa)	Young's modulus	1.1 [81]
ν	Poisson's ratio	0.365 [81]
α (ppmK^{-1})	Coefficient of thermal expansion	104 *
E-glass fibre		
E (GPa)	Young's modulus	72 [82]
ν	Poisson's ratio	0.21 [82]
α (ppmK^{-1})	Coefficient of thermal expansion	5.0 [8282]
Elium® 188 XO (polymerized)		
E (GPa)	Young's modulus	3.17 [83]
ν	Poisson's ratio	0.22**
α (ppmK^{-1})	Coefficient of thermal expansion	65 [83]
Glass fibre/PMMA substrate		
E_1 (GPa)	Longitudinal Young's modulus	38.89 [53]
E_2, E_3 (GPa)	Transverse Young's modulus	17.43 [53]
G_{12}, G_{13} (GPa)	In-Plane shear modulus	9.05 [53]
G_{23} (GPa)	Out-of-plane shear modulus	7.2 **
ν_{12}, ν_{13}	Major in-plane Poisson's ratio	0.217 [53]
ν_{23}, ν_{32}	Minor in-plane Poisson's ratio	0.216 **
α_1 (ppmK^{-1})	Coefficient of thermal expansion (longitudinal)	7.2 **
α_2 (ppmK^{-1})	Coefficient of thermal expansion (transverse)	44 **

*Value provided by supplier.
**Calculated value.

The stress state for the simulation of the DCB specimen with a bond line thickness of 0.25 mm is shown in Fig. 25. The peak residual stress in the adhesive layer was determined to be 9.1 MPa, which is slightly over 50 % of the reported ultimate tensile strength of the MMA adhesive (16 MPa – 18 MPa) [55]. Daghyani [84] observed crack tip instability in carbon fibre reinforced plastic composite substrates bonded with an epoxy adhesive when the thermal residual stress was 33 % of the adhesive strength. Thus, the residual stress in the adhesive layer of the DCB specimen may have surpassed the threshold for crack tip instability, causing the observed crack tip

oscillations at LT conditions (Fig. 19).

A summary of the peak residual stresses for the simulations of the DCB and ENF specimens are found in Table 12 and Table 13. It can be shown that the predicted thermal residual stresses for all bond-line thicknesses relative to the ultimate tensile strength are higher than the values reported by Daghyani [84]. Finite element simulations show that the thermal residual stresses decrease slightly with increasing bond-line thickness, although Akhavan-Safar et al. [74] reported an increase in T-stress (leading to increasing crack tip instability) with increasing bond-line thickness. However, Akhavan-Safar et al. [74] also modeled an optimum bond-line thickness to maximize G_{IC} taking into consideration substrate thickness. Thus, thermal residual stresses may assist as a first order estimation for crack tip instability before considering more robust modeling techniques.

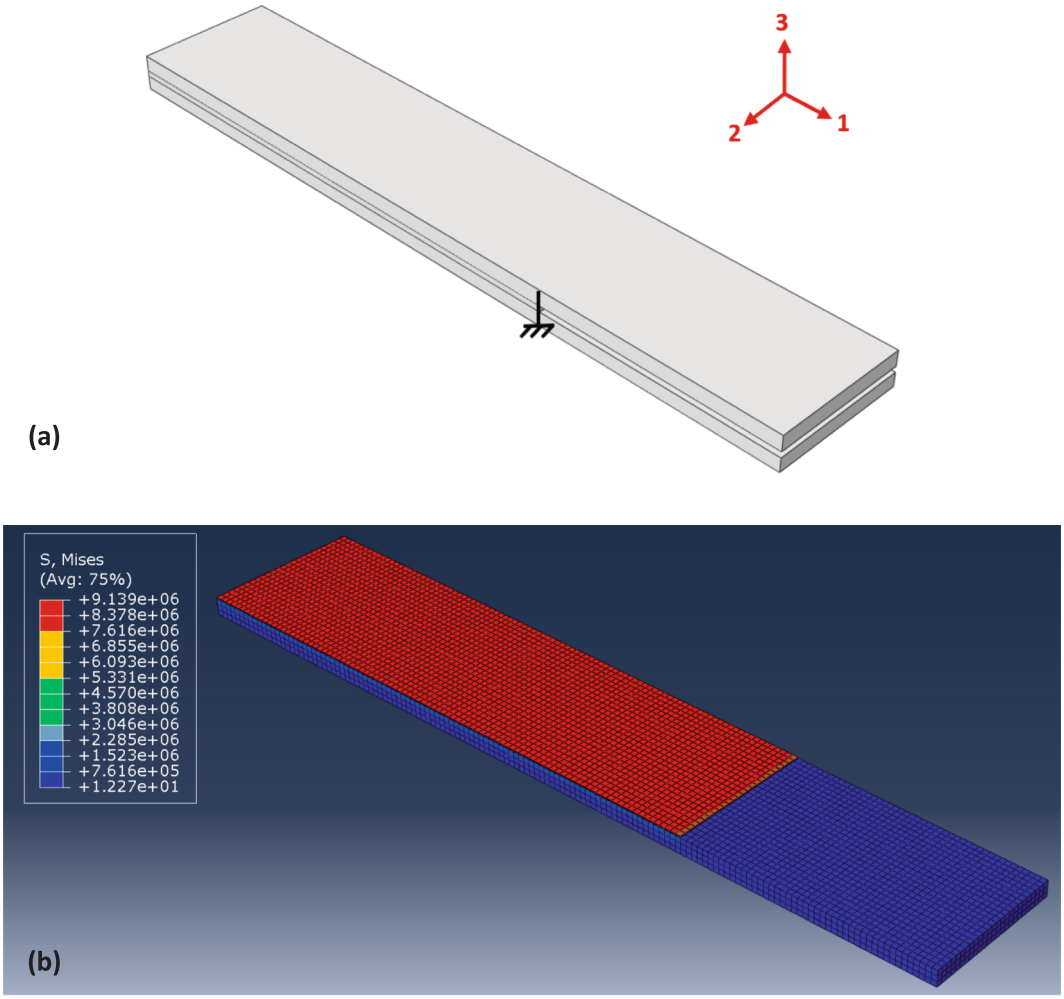

Fig. 25. Thermal expansion simulation showing: (a) free body diagram of DCB joint with encastre boundary condition at single point (with temperature variation applied by propagating a predefined field) and (b) simulated stress state (Von Mises, units MPa) after cooldown to −40 °C for DCB specimen with a bond line thickness of 0.25 mm. The peak stress within the adhesive layer was found to be 9.1 MPa.

Table 12
Thermal residual stresses during cooling process for DCB specimens computed via finite element method.

Bond-line Thickness (mm)	Peak Residual Stress (MPa)
0.25	9.139
0.635	8.673
0.8	8.647

Table 13
Thermal residual stresses during cooling process for ENF specimens computed via finite element method.

Bond-line Thickness (mm)	Peak Residual Stress (MPa)
0.25	9.053
0.475	8.683
0.625	8.673

Data availability

Data will be made available on request.

References

[1] Kazemi ME, Shanmugam L, Lu D, Wang X, Wang B, Yang J. Mechanical properties and failure modes of hybrid fiber reinforced polymer composites with a novel liquid thermoplastic resin, Elium®. Compos Part A Appl Sci Manuf Oct. 2019;125:105523. https://doi.org/10.1016/j.compositesa.2019.105523.

[2] Bhudolia SK, Gohel G, Kantipudi J, Leong KF, Gerard P. Mechanical performance and damage mechanisms of thin rectangular carbon/ Elium® tubular thermoplastic composites under flexure and low-velocity impact. Thin-Walled Struct Aug. 2021;165:107971. https://doi.org/10.1016/j.tws.2021.107971.

[3] Murray RE, et al. Structural validation of a thermoplastic composite wind turbine blade with comparison to a thermoset composite blade. Renew Energy Feb. 2021;164:1100–7. https://doi.org/10.1016/j.renene.2020.10.040.

[4] Barbosa LCM, Bortoluzzi DB, Ancelotti AC. Analysis of fracture toughness in mode II and fractographic study of composites based on Elium® 150 thermoplastic matrix. Compos B Engng Oct. 2019;175:107082. https://doi.org/10.1016/j.compositesb.2019.107082.

[5] Bhudolia SK, Gohel G, Vasudevan D, Leong KF, Gerard P. On the Mode II fracture toughness, failure, and toughening mechanisms of wholly thermoplastic composites with ultra-lightweight thermoplastic fabrics and innovative Elium® resin. Compos Part A Appl Sci Manuf Oct. 2022;161:107115. https://doi.org/10.1016/j.compositesa.2022.107115.

[6] Ramezani F, Ayatollahi MR, Akhavan-Safar A, da Silva LFM. A comprehensive experimental study on bi-adhesive single lap joints using DIC technique. Int J Adhes Adhes Oct. 2020;102:102674. https://doi.org/10.1016/j.ijadhadh.2020.102674.

[7] Scarselli G, Quan D, Murphy N, Deegan B, Dowling D, Ivankovic A. Adhesion Improvement of Thermoplastics-Based Composites by Atmospheric Plasma and UV Treatments. Applied Composite Materials Feb. 2021;28(1):71–89. https://doi.org/10.1007/s10443-020-09854-y.

[8] W. Seneviratne, J. Tomblin, and B. Saathoff, "Thermoplastic Joining Materials Guidance for Aircraft Design and Certification," Sep. 29, 2021, *Wichita State University, Wichita*.

[9] Zhang J, de Souza M, Creighton C, Varley RJ. New approaches to bonding thermoplastic and thermoset polymer composites. Compos Part A Appl Sci Manuf Jun. 2020;133:105870. https://doi.org/10.1016/j.compositesa.2020.105870.

[10] Yildirim C, Ulus H, Beylergil B, Al-Nadhari A, Topal S, Yildiz M. Tailoring adherend surfaces for enhanced bonding in CF/PEKK composites: Comparative analysis of atmospheric plasma activation and conventional treatments. Compos Part A Appl Sci Manuf May 2024;180:108101. https://doi.org/10.1016/j.compositesa.2024.108101.

[11] Yildirim C, Ulus H, Beylergil B, Al-Nadhari A, Topal S, Yildiz M. Effect of atmospheric plasma treatment on Mode-I and Mode-II fracture toughness properties of adhesively bonded carbon fiber/PEKK composite joints. Engng Fract Mech Sep. 2023;289:109463. https://doi.org/10.1016/j.engfracmech.2023.109463.

[12] Kaybal HB, Ulus H. Comparative analysis of thermoplastic and thermoset adhesives performance and the influence on failure analysis in jointed <scp>elium</scp> -based composite structures. Polym Compos Mar. 2024;45(4):3474–92. https://doi.org/10.1002/pc.28003.

[13] Brockmann W, Geiß PL, Klingen J, Schröder B. Adhesive Bonding. Wiley 2008. https://doi.org/10.1002/9783527623921.

[14] Baldan A. Adhesively-bonded joints and repairs in metallic alloys, polymers and composite materials: Adhesives, adhesion theories and surface pretreatment. J Mater Sci Jan. 2004;39(1):1–49. https://doi.org/10.1023/B:JMSC.0000007726.58758.e4.

[15] Marques A, et al. Review on Adhesives and Surface Treatments for Structural Applications: Recent Developments on Sustainability and Implementation for Metal and Composite Substrates. Materials Dec. 2020;13(24):5590. https://doi.org/10.3390/ma13245590.

[16] J. (JP) Huang and J. Lean. Advances in acrylic structural adhesives," in *Advances in Structural Adhesive Bonding*. Elsevier 2023:69–101. https://doi.org/10.1016/B978-0-323-91214-3.00010-7.

[17] Aronovich DA, Boinovich LB. "Structural Acrylic Adhesives: A Critical Review," in *Progress in Adhesion and Adhesives*. Wiley 2021:651–708. https://doi.org/10.1002/9781119846703.ch15.

[18] Murray RE, Roadman J, Beach R. Fusion joining of thermoplastic composite wind turbine blades: Lap-shear bond characterization. Renew Energy Sep. 2019;140:501–12. https://doi.org/10.1016/j.renene.2019.03.085.

[19] Murray RE, Jenne S, Snowberg D, Berry D, Cousins D. Techno-economic analysis of a megawatt-scale thermoplastic resin wind turbine blade. Renew Energy Feb. 2019;131:111–9. https://doi.org/10.1016/j.renene.2018.07.032.

[20] Obande W, Brádaigh CMÓ, Ray D. Continuous fibre-reinforced thermoplastic acrylic-matrix composites prepared by liquid resin infusion – A review. Compos B Engng Jun. 2021;215:108771. https://doi.org/10.1016/j.compositesb.2021.108771.

[21] Dehaghani R. Experimental and Numerical Assessment of Adhesively Bonded Non-Crimp Fabric Carbon Fiber/Epoxy Composite Joints. Waterloo: University of Waterloo; 2021. MASc Thesis.

[22] "Test Method for Mode I Interlaminar Fracture Toughness of Unidirectional Fiber-Reinforced Polymer Matrix Composites," Oct. 01, 2013, *ASTM International, West Conshohocken, PA*. doi: 10.1520/D5528-13.

[23] "Test Method for Determination of the Mode II Interlaminar Fracture Toughness of Unidirectional Fiber-Reinforced Polymer Matrix Composites," Mar. 15, 2019, *ASTM International, West Conshohocken, PA*. doi: 10.1520/D7905_D7905M-19E01.

[24] Devine M, Bajpai A, Brádaigh CMÓ, Ray D. 'Resin welding': A novel route to joining acrylic composite components at room temperature. Compos B Engng Mar. 2024;272:111212. https://doi.org/10.1016/j.compositesb.2024.111212.

[25] Bhudolia SK, Gohel G, Leong KF, Barsotti RJ. Investigation on Ultrasonic Welding Attributes of Novel Carbon/Elium® Composites. Materials Mar. 2020;13(5):1117. https://doi.org/10.3390/ma13051117.

[26] Reis JP, de Moura MFSF, Moreira RDF. Extension of the crack equivalent method applied to mode II fracture of thermoplastic composites bonded joints using the ENF test. Compos Struct Jan. 2025;352:118687. https://doi.org/10.1016/j.compstruct.2024.118687.

[27] Moller J, Hunter R, Molina J, Vizán A, Peréz J, da Silva LFM. Influence of the temperature on the fracture energy of a methacrylate adhesive for mining applications. Appl Adhes Sci Dec. 2015;3(1):14. https://doi.org/10.1186/s40563-015-0041-5.

[28] Banea MD, da Silva LFM. The effect of temperature on the mechanical properties of adhesives for the automotive industry. Proceedings of the Institution of Mechanical Engineers, Part L: Journal of Materials: Design and Applications Apr. 2010;224(2):51–62. https://doi.org/10.1243/14644207JMDA283.

[29] S. Takayuki, J. He, and S. Aso, "Study of Cryogenic Mechanical Strength and Fracture Behavior of Adhesives for CFRP Tanks of Reusable Launch Vehicles," *Memoirs of the Faculty of Engineering, Kyushu University*, vol. 66, Feb. 2006.

[30] Zhang Y, Vassilopoulos AP, Keller T. Effects of low and high temperatures on tensile behavior of adhesively-bonded GFRP joints. Compos Struct Jun. 2010;92 (7):1631–9. https://doi.org/10.1016/j.compstruct.2009.11.028.

[31] Rahmani A, Choupani N. Experimental and numerical analysis of fracture parameters of adhesively bonded joints at low temperatures. Engng Fract Mech Feb. 2019;207:222–36. https://doi.org/10.1016/j.engfracmech.2018.12.031.

[32] Brito CBG, Sales RCM, Donadon MV. Effects of temperature and moisture on the fracture behaviour of composite adhesive joints. Int J Adhes Adhes Jul. 2020; 100:102607. https://doi.org/10.1016/j.ijadhadh.2020.102607.

[33] Abdel-Monsef S, Renart J, Carreras L, Turon A, Maimí P. Effect of environment conditioning on mode II fracture behaviour of adhesively bonded joints. Theor Appl Fract Mech Apr. 2021;112:102912. https://doi.org/10.1016/j.tafmec.2021.102912.

[34] Kang S-G, Kim M-G, Kim C-G. Evaluation of cryogenic performance of adhesives using composite–aluminum double-lap joints. Compos Struct May 2007;78(3): 440–6. https://doi.org/10.1016/j.compstruct.2005.11.005.

[35] Abdel-Monsef S, Renart J, Carreras L, Maimí P, Turon A. Effect of environmental conditioning on pure mode I fracture behaviour of adhesively bonded joints. Theor Appl Fract Mech Dec. 2020;110:102826. https://doi.org/10.1016/j.tafmec.2020.102826.

[36] Yildirim C, Ulus H, Sas HS, Topal S, Yildiz M. Assessing the fracture and dynamic mechanical performance of CF/PEKK joints bonded with epoxy-based adhesive film for aerospace applications: Impact of thermal and cycling hygrothermal conditions. Compos Part A Appl Sci Manuf Mar. 2025;190:108659. https://doi.org/10.1016/j.compositesa.2024.108659.

[37] Senol H, Ulus H, Yildirim C, Al-Nadhari A, Topal S, Yildiz M. Assessing fracture toughness performance of adhesively bonded carbon fiber/epoxy composite joints accompanied by acoustic emission inspection: Effect of surface treatment methods. Engng Fract Mech May 2025;321:111119. https://doi.org/10.1016/j.engfracmech.2025.111119.

[38] Crocombe AD. Global yielding as a failure criterion for bonded joints. Int J Adhes Adhes Jul. 1989;9(3):145–53. https://doi.org/10.1016/0143-7496(89)90110-3.

[39] Arenas JM, Narbón JJ, Alía C. Optimum adhesive thickness in structural adhesives joints using statistical techniques based on Weibull distribution. Int J Adhes Adhes Apr. 2010;30(3):160–5. https://doi.org/10.1016/j.ijadhadh.2009.12.003.

[40] da Silva LFM, Rodrigues TNSS, Figueiredo MAV, de Moura MFSF, Chousal JAG. Effect of Adhesive Type and Thickness on the Lap Shear Strength. J Adhes Nov. 2006;82(11):1091–115. https://doi.org/10.1080/00218460600948511.

[41] Watson B, Worswick MJ, Cronin DS. Quantification of mixed mode loading and bond line thickness on adhesive joint strength using novel test specimen geometry. Int J Adhes Adhes Oct. 2020;102:102682. https://doi.org/10.1016/j.ijadhadh.2020.102682.

[42] Manterola J, et al. Effect of the width-to-thickness ratio on the mode I fracture toughness of flexible bonded joints. Engng Fract Mech Sep. 2019;218:106584. https://doi.org/10.1016/j.engfracmech.2019.106584.

[43] de Freitas ST, Budzik MK. "Bondline thickness: Fracture mechanics perspective," in *Advances in Structural Adhesive Bonding*. Elsevier 2023:615–41. https://doi.org/10.1016/B978-0-323-91214-3.00027-2.

[44] Banea MD, da Silva LFM, Campilho RDSG. The Effect of Adhesive Thickness on the Mechanical Behavior of a Structural Polyurethane Adhesive. J Adhes Jan. 2015;91(5):331–46. https://doi.org/10.1080/00218464.2014.903802.

[45] da Silva LFM, de Magalhães FACRG, Chaves FJP, de Moura MFSF. Mode II Fracture Toughness of a Brittle and a Ductile Adhesive as a Function of the Adhesive Thickness. J Adhes Aug. 2010;86(9):891–905. https://doi.org/10.1080/00218464.2010.506155.

[46] Castagnetti D, Spaggiari A, Dragoni E. Effect of Bondline Thickness on the Static Strength of Structural Adhesives Under Nearly-Homogeneous Shear Stresses. J Adhes Jul. 2011;87(7–8):780–803. https://doi.org/10.1080/00218464.2011.597309.

[47] Nam S, Yu YH, Choi I, Bang CS, Lee DG. Fracture toughness improvement of polyurethane adhesive joints with chopped glass fibers at cryogenic temperatures. Compos Struct Jan. 2014;107:522–7. https://doi.org/10.1016/j.compstruct.2013.08.015.

[48] Jia Z, Yuan G, Hui D, Feng X, Zou Y. Effect of high loading rate and low temperature on mode I fracture toughness of ductile polyurethane adhesive. J Adhes Sci Technol Jan. 2019;33(1):79–92. https://doi.org/10.1080/01694243.2018.1546364.

[49] Jia Z, Yuan G, Feng X, Zou Y, Yu J. Shear properties of polyurethane ductile adhesive at low temperatures under high strain rate conditions. Compos B Engng Jan. 2019;156:292–302. https://doi.org/10.1016/j.compositesb.2018.08.060.

[50] Jia Z, Yuan G, Hui D, Feng X, Zou Y. Effect of high strain rate and low temperature on mode II fracture toughness of ductile adhesive. Int J Adhes Adhes Nov. 2018;86:105–12. https://doi.org/10.1016/j.ijadhadh.2018.09.003.

[51] Ribas M, et al. Exploring strain rate variation in the adhesive layer during constant speed mode I fracture tests: Loading speed and test temperature effects. Theor Appl Fract Mech Apr. 2024;130:104274. https://doi.org/10.1016/j.tafmec.2024.104274.

[52] Hayashi A, Sekiguchi Y, Sato C. Effect of temperature and loading rate on the mode I fracture energy of structural acrylic adhesives. Journal of Advanced Joining Processes Jun. 2022;5:100079. https://doi.org/10.1016/j.jajp.2021.100079.

[53] E. Shi and J. Montesano, "Effect of low temperature on the mechanical properties and failure characteristics of an infused non-crimp fabric glass fiber-reinforced reactive thermoplastic.," *Submitted (under review)*.

[54] Zivkovic M. Manufacturing of a Fiber-Reinforced Thermoplastic Composite Micro-Generating Wind Turbine Blade. Waterloo: University of Waterloo; 2023. MASc Thesis.

[55] "Bostik FIT30 45 TWO COMPONENT METHACRYLATE - Technical Datasheet," Dec. 09, 2019, *AEC Polymers, Le Barp*.

[56] Edwards BK. Composite Manufacturing of Small Wind Turbine Blades. San Luis Obispo: Faculty of California Polytechnic State University; 2009. Masters Thesis.

[57] Verma AS, Vedvik NP, Gao Z, Castro SGP, Teuwen JJE. Bondline Thickness Effects on Damage Tolerance of Adhesive Joints Subjected to Localized Impact Damages: Application to Leading Edge of Wind Turbine Blades. Materials Dec. 2021;14(24):7526. https://doi.org/10.3390/ma14247526.

[58] Sayer F, Antoniou A, van Wingerde A. Investigation of structural bond lines in wind turbine blades by sub-component tests. Int J Adhes Adhes Sep. 2012;37: 129–35. https://doi.org/10.1016/j.ijadhadh.2012.01.021.

[59] Campilho R, Ribeiro J, Rocha R, Leal A, Viana F. Validation of fracture envelopes of structural adhesives for mixed-mode strength prediction of bonded joints. Frattura ed Integrità Strutturale Mar. 2019;13(48):332–47. https://doi.org/10.3221/IGF-ESIS.48.32.

[60] Blackman BRK, Kinloch AJ, Paraschi M, Teo WS. Measuring the mode I adhesive fracture energy, GIC, of structural adhesive joints: the results of an international round-robin. Int J Adhes Adhes Jan. 2003;23(4):293–305. https://doi.org/10.1016/S0143-7496(03)00047-2.

[61] P. Gálvez, R. Carbas, R. Campilho, J. Abenojar, M. Martínez, and da S. LFM, "Fracture toughness in Mode I (G_{IC}) for ductile adhesives," *J Phys Conf Ser*, vol. 843, p. 012008, May 2017, doi: 10.1088/1742-6596/843/1/012008.

[62] D. Brown, W. Christian, and R. M. Hanson, "Tracker Video Analysis and Modeling Tool," 2023, *Free Software Foundation, Inc.*

[63] Yoshimura A, Takaki T, Noji Y, Yokozeki T, Ogasawara T, Ogihara S. Fracture Toughness of CFRP Adhesive Bonded Joints at Cryogenic Temperature. J Adhes Sci Technol Apr. 2012;26(7):1017–31. https://doi.org/10.1163/156856111X593694.

[64] Santos MAS, Campilho RDSG. Mixed-mode fracture analysis of composite bonded joints considering adhesives of different ductility. Int J Fract Sep. 2017;207 (1):55–71. https://doi.org/10.1007/s10704-017-0219-x.

[65] Oshima S, Koyanagi J. Review on Damage and Failure in Adhesively Bonded Composite Joints: A Microscopic Aspect. Polymers (Basel) Jan. 2025;17(3):377. https://doi.org/10.3390/polym17030377.

[66] R. Lopes Fernandes, S. Teixeira de Freitas, M. K. Budzik, J. A. Poulis, and R. Benedictus, "From thin to extra-thick adhesive layer thicknesses: Fracture of bonded joints under mode I loading conditions," *Eng Fract Mech*, vol. 218, p. 106607, Sep. 2019, doi: 10.1016/j.engfracmech.2019.106607.

[67] Kinloch AJ, Shaw SJ. The Fracture Resistance of a Toughened Epoxy Adhesive. J Adhes May 1981;12(1):59–77. https://doi.org/10.1080/00218468108071189.

[68] Campilho RDSG, Moura DC, Banea MD, da Silva LFM. Adhesive thickness effects of a ductile adhesive by optical measurement techniques. Int J Adhes Adhes Mar. 2015;57:125–32. https://doi.org/10.1016/j.ijadhadh.2014.12.004.

[69] Saleh MN, Budzik MK, Saeedifar M, Zarouchas D, Teixeira De Freitas S. On the influence of the adhesive and the adherend ductility on mode I fracture characterization of thick adhesively-bonded joints. Int J Adhes Adhes Jun. 2022;115:103123. https://doi.org/10.1016/j.ijadhadh.2022.103123.
[70] Sekiguchi Y, Sato C. Experimental investigation of the effects of adhesive thickness on the fracture behavior of structural acrylic adhesive joints under various loading rates. Int J Adhes Adhes Mar. 2021;105:102782. https://doi.org/10.1016/j.ijadhadh.2020.102782.
[71] Pardoen T, Ferracin T, Landis CM, Delannay F. Constraint effects in adhesive joint fracture. J Mech Phys Solids Sep. 2005;53(9):1951–83. https://doi.org/10.1016/j.jmps.2005.04.009.
[72] Melcher RJ, Johnson WS. Mode I fracture toughness of an adhesively bonded composite–composite joint in a cryogenic environment. Compos Sci Technol Mar. 2007;67(3–4):501–6. https://doi.org/10.1016/j.compscitech.2006.08.026.
[73] Chen B, Dillard DA. The effect of the T-stress on crack path selection in adhesively bonded joints. Int J Adhes Adhes Jan. 2001;21(5):357–68. https://doi.org/10.1016/S0143-7496(01)00011-2.
[74] Akhavan-Safar A, Ayatollahi MR, Moazzami M, da Silva LFM. The role of T-stress and stress triaxiality combined with the geometry on tensile fracture energy of brittle adhesives. Int J Adhes Adhes Dec. 2018;87:12–21. https://doi.org/10.1016/j.ijadhadh.2018.09.008.
[75] R. Lopes Fernandes, S. Teixeira de Freitas, M. K. Budzik, J. A. Poulis, and R. Benedictus, "Role of adherend material on the fracture of bi-material composite bonded joints," *Compos Struct*, vol. 252, p. 112643, Nov. 2020, doi: 10.1016/j.compstruct.2020.112643.
[76] R. Lopes Fernandes, M. K. Budzik, R. Benedictus, and S. Teixeira de Freitas, "Multi-material adhesive joints with thick bond-lines: Crack onset and crack deflection," *Compos Struct*, vol. 266, p. 113687, Jun. 2021, doi: 10.1016/j.compstruct.2021.113687.
[77] Omairey S, Jayasree N, Kazilas M. Defects and uncertainties of adhesively bonded composite joints. SN Appl Sci Sep. 2021;3(9):769. https://doi.org/10.1007/s42452-021-04753-8.
[78] Avendaño R, Carbas RJC, Marques EAS, da Silva LFM, Fernandes AA. Effect of temperature and strain rate on single lap joints with dissimilar lightweight adherends bonded with an acrylic adhesive. Compos Struct Sep. 2016;152:34–44. https://doi.org/10.1016/j.compstruct.2016.05.034.
[79] R. M. Jones, *Mechanics of Composite Materials*. CRC Press, 2018. doi: 10.1201/9781498711067.
[80] Schapery RA. Thermal Expansion Coefficients of Composite Materials Based on Energy Principles. J Compos Mater Jul. 1968;2(3):380–404. https://doi.org/10.1177/002199836800200308.
[81] Kozłowski M, Bula A, Hulimka J. Determination of Mechanical Properties of Methyl Methacrylate Adhesive (MMA). Architecture, Civil Engineering, Environment Jan. 2018;11(3):87–96. https://doi.org/10.21307/acee-2018-041.
[82] Agarwal BD, Broutman LJ, Chandrashekhara K. *Analysis and performance of fiber composites*. 4th ed. Nashville, TN: John Wiley & Sons; 2017.
[83] "Liquid thermoplastic resin for tougher composites," *Arkema, Colombes Cedex*.
[84] Daghyani HR, Ye L, Mai Y-W. Effect of thermal residual stress on the crack path in adhesively bonded joints. J Mater Sci May 1996;31(10):2523–9. https://doi.org/10.1007/BF00687277.